Designing Functional Architectures for Soft Robotics

University of Turku
Department of Mechanical and Materials Engineering
Master of Science (Tech) Thesis
Mechanical and Materials Engineering
June 2026
Muhammad Nafay

UNIVERSITY OF TURKU
Department of Mechanical and Materials Engineering

Muhammad Nafay: Designing Functional Architectures for Soft Robotics

Master of Science (Tech) Thesis, 94 p.
Mechanical and Materials Engineering
June 2026

Soft robotics enables compliant and safe interaction in complex and continuum environments; however, the integration of reliable, electronics-free sensing remains a major challenge for fully pneumatic robotic systems. Current pneumatic strain gauges predominantly employ simple microchannel geometries, which limit pressure sensitivity, structural efficiency, and spatial sensing capability.
This thesis investigates the use of gyroid-based Triply Periodic Minimal Surface (TPMS) architectures as internal structures for pneumatic tactile sensing, with the aim of overcoming limitations in conventional pressure sensing approaches. Parametric gyroid geometries were designed using computational methods, and their mechanical response under loading was initially evaluated through finite element analysis (FEA). In addition, an experimental proof-of-concept setup was developed, integrating multiple pressure gauges within a pneumatic network to capture real-time pressure variations under different touch-points.
A soft pneumatic sensing system was developed and experimentally evaluated to assess pressure sensitivity and response behavior under various loads. The results indicate that the gyroid structure enables measurable and distinguishable pressure changes across multiple sensing touch points, when changes in internal flow due to structural deformation. While variations in sensor response were observed depending on touch-point location and loading conditions. These findings demonstrate that TPMS architectures can improve pneumatic sensing response by overcoming the drawbacks such as leakage, ballooning effect, and the global pressure response in the traditional pressure sensors.

Keywords: soft robotics; tactile perception; pneumatic sensors; gyroid architectures; electronics-free soft robots

Contents

List of Figures

List of Tables

List of Acronyms

AM	Additive Manufacturing
CAD	Computer-Aided Design
FE	Finite Element
FEA	Finite Element Analysis
FDM	Fused Deposition Modeling
IPA	Isopropyl Alcohol
PDMS	Polydimethylsiloxane
POC	Proof of Concept
SLA	Stereolithography
STL	Standard Tessellation Language
TPMS	Triply Periodic Minimal Surface
TPU	Thermoplastic Polyurethane

1 Introduction

1.1 Background

Soft robotics is an emerging field of robotics that focuses on the design and control of systems made from compliant and deformable materials. Unlike conventional rigid robots, soft robots can undergo large elastic deformation, allowing safer interaction with humans, fragile objects, and unstructured environments [1]. This compliance makes soft robots suitable for applications where adaptability, safe contact, and flexible motion are required. The development of soft robotics is connected to bio-inspired engineering [2]. Many biological systems, such as octopus arms, worms, fish, and human muscles, can deform continuously and adapt their shape during movement or interaction with the environment [3]. These natural systems have inspired the development of soft robotic structures that use flexible materials and distributed deformation instead of rigid joints and links.

1.1.1 Soft Robots

Soft robots can be designed in many different forms depending on their intended function, actuation method, and biological inspiration. The following examples are introduced to show how bio-inspired principles have been used in different soft robotic systems.

Multigait soft robots are one example of bio-inspired soft robotic systems. These robots can perform different locomotion modes, such as crawling, bending, and turning, through the controlled deformation of soft materials. Their movement is inspired by organisms such as worms and octopus arms, which use compliant body structures to adapt to different environments [3].

Soft robotic grippers are another important example. The Harvard soft gripper was inspired by the adaptive grasping ability of biological fingers and tentacle-like structures [4]. It uses pneumatic networks embedded inside soft elastomeric materials, where injected air pressure causes controlled bending of the fingers. This allows the gripper to safely grasp delicate and irregularly shaped objects.

Octopus-inspired continuum arms have also been developed to reproduce the flexible motion of octopus tentacles. These systems replicate the idea of a muscular hydrostat structure, enabling continuous bending and flexible manipulation without rigid skeletal components [5]. Such designs are useful for movement in confined or unstructured environments.

Fish-like swimming robots are inspired by the undulatory motion of aquatic organisms such as fish and rays [6]. In these systems, soft fluidic elastomer actuators generate controlled body deformation, producing propulsion and manoeuvrability underwater. In addition, soft wearable exosuits have been developed based on the biomechanics of human muscles and joints to support natural body movement during rehabilitation and mobility assistance [7].

These examples show that soft robots are particularly suitable for applications requiring compliant interaction, adaptive motion, and safe contact. In robotic manipulation, soft grippers can conform to objects with different shapes and fragility, allowing stable grasping without complex rigid mechanisms [8]. In healthcare and rehabilitation, the flexibility of soft robotic systems enables safer interaction with the human body during assistive and therapeutic applications [7].

A major reason for the development of soft robots is their ability to produce large deformation while maintaining safety and adaptability. In conventional rigid robots, actuation, sensing, control, and power delivery are often based on electrical and mechanical systems. In contrast, many soft robots rely on fluidic actuation, especially pneumatic actuation, because pressurized air can produce controlled deformation in compliant structures [9]–[11]. The successful use of soft pneumatic actuators has also encouraged the use of fluidic principles in soft robotic control and sensing systems [12]–[15].

Soft pneumatic grippers have become an important class of end-effectors in soft robotics due to their simple mechanical structure, high compliance, inherent safety, low manufacturing cost, and adaptive motion characteristics [16]–[18]. Unlike rigid grippers, soft pneumatic grippers are typically fabricated from elastomeric materials such as silicone rubber or other polymer-based compounds. These materials allow the gripper to undergo large deformation and conform to objects with different shapes, sizes, and surface conditions [3].

The behaviour of soft pneumatic grippers is biologically inspired because they can bend, wrap, and adapt around objects in a manner similar to natural soft manipulators, such as human fingers or octopus arms. This compliant deformation enables gentle and stable interaction without requiring complex rigid joints or mechanisms [19], [20].

Despite these advantages, sensing deformation and contact force remains a significant challenge in soft pneumatic grippers [21], [22]. Since these systems experience large strain during actuation and contact, embedded sensors must remain flexible, stretchable, and mechanically compatible with the soft body. If the sensor is too stiff or poorly integrated, it can restrict the natural deformation of the gripper and reduce its overall performance.

Therefore, sensing in soft pneumatic grippers should be considered together with the mechanical design of the soft structure. A suitable sensing approach must detect contact or pressure while preserving the compliance and deformation behaviour of the gripper. This requirement motivates the development of soft, integrated, and mechanically compatible sensing methods for pneumatic gripper systems.

1.1.2 Additive Manufacturing for Soft Robots

Additive Manufacturing (AM) offers several advantages compared to conventional fabrication methods. One of the main advantages of AM is its ability to produce complex geometries that are difficult or impossible to manufacture using traditional machining processes. Features such as internal channels, interwoven structures, and complex curved surfaces can be fabricated directly from computer-aided design (CAD) models without the need for additional tooling.

This design freedom allows more efficient and lightweight components to be produced while reducing material waste [23].

In addition, AM simplifies post-processing and assembly requirements, as complex parts can often be 3D printed as a single component rather than being assembled from multiple parts. These advantages make AM a flexible and efficient manufacturing approach for modern engineering applications [24].

Stereolithography (SLA) is a vat photopolymerization-based AM process in which a liquid photopolymer resin is selectively cured layer by layer using a light source. In this method, the three-dimensional model is first prepared digitally, after which supports are generated and the part is printed by curing successive resin layers. After printing, the part normally requires washing, support removal, and post-curing to obtain the final component.

Figure 1.1 shows the SLA-based 3D printing workflow followed in this study. The workflow begins with design and material selection, followed by support generation and printing. After printing, the part undergoes post-processing steps, including washing, support removal, and curing, before the final printed component is ready for use.

Figure 1.1: Schematic representation of the stereolithography (SLA) 3D printing workflow used in this study.

These benefits are particularly important in the field of soft robotics. Soft robotic systems require flexible and compliant structures that can undergo large deformations and interact safely with humans and unstructured environments. Conventional fabrication methods such as molding and machining often limit geometric complexity and make it difficult to integrate internal features like channels or graded stiffness regions. AM overcomes these challenges by enabling the fabrication of soft robotic components with complex shapes and mechanical behavior directly from CAD models [25].

Furthermore, AM allows the production of application-specific components, where geometry and dimensions can be adjusted based on functional requirements. Such flexibility is difficult to achieve using conventional manufacturing methods and is particularly beneficial for prototyping and experimental work in soft robotics.

Multi-material additive manufacturing extends these advantages by enabling different materials or material properties to be combined within the same printed structure. This can be useful when a component requires regions with different stiffness, flexibility, conductivity, or functional behaviour.

Figure 1.2 shows an overview of multi-material additive manufacturing strategies and the related possibilities for property enhancement. The figure includes manufacturing approaches such as material extrusion, vat photopolymerization, powder bed fusion (PBF), Fused Filament Fabrication (FFF), binder jetting (BJ), directed energy deposition (DED), sheet lamination (SL), and material jetting, together with different ways of improving component performance through material combination and functional integration.

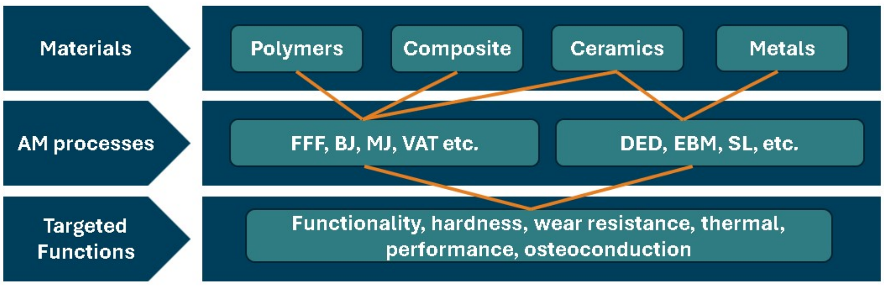

Figure 1.2: Overview of manufacturing and property enhancement possibilities of multi-material additive manufacturing, modified from [26].

One of the most important advantages of AM is the reduction or elimination of tooling requirements. Conventional fabrication usually depends on molds, dies, and fixtures, which are expensive and time-consuming to produce, especially for low-volume manufacturing. AM enables parts to be fabricated directly from CAD models, removing the need for dedicated tooling. This capability reduces manufacturing lead time and allows faster design changes without major cost penalties, which are common limitations of traditional manufacturing methods [27], [28].

AM also provides major advantages through part consolidation and simplified assembly. Components that would normally be produced as multiple individual parts can often be fabricated as a single integrated structure. This reduces assembly time, lowers the risk of manufacturing errors, and improves overall reliability. In soft robotics, this is particularly useful because actuators, internal cavities, compliant structures, and sensing regions often need to be integrated within compact and deformable components.

Another key advantage of AM is its ability to support customized and low-volume production. Instead of relying on large-scale tooling and centralized production, AM allows components to be produced directly from digital CAD files when design changes are required. This reduces inventory requirements, shortens development cycles, and makes AM suitable for experimental prototypes and application-specific parts [29].

These advantages are especially relevant in soft robotics, where the design architecture strongly influences mechanical behaviour, durability, and functional performance. Soft robotic components rely on compliant structures that must deform repeatedly while maintaining stable and predictable motion. Therefore, the ability of AM to fabricate complex geometries directly from CAD models is important for developing soft robotic devices.

With the advancement of AM, it has become possible to fabricate complex internal architectures that are difficult or impractical to manufacture using conventional methods. This allows mechanical properties to be controlled not only through material selection, but also through geometry. As a result, lattice-based and other architected structures can be used in soft robotics to adjust stiffness, deformation behaviour, and functional response.

1.1.3 Design Architectures

Lattice structures are one of the most commonly used design architectures due to their low weight and tunable stiffness. These structures are typically composed of repeating unit cells made up of struts and nodes.

Figure 1.3 shows a BCC Lattice block, where the structure is formed by the periodic arrangement of interconnected struts and nodes. Figure 1.3(i) illustrates the complete lattice network, while Figure 1.3(ii) highlights the basic structural elements. The struts are the elongated members that transfer mechanical loads through the lattice, whereas the nodes are the intersection points where multiple struts meet. The arrangement of these struts and nodes controls the mechanical response of the lattice structure.

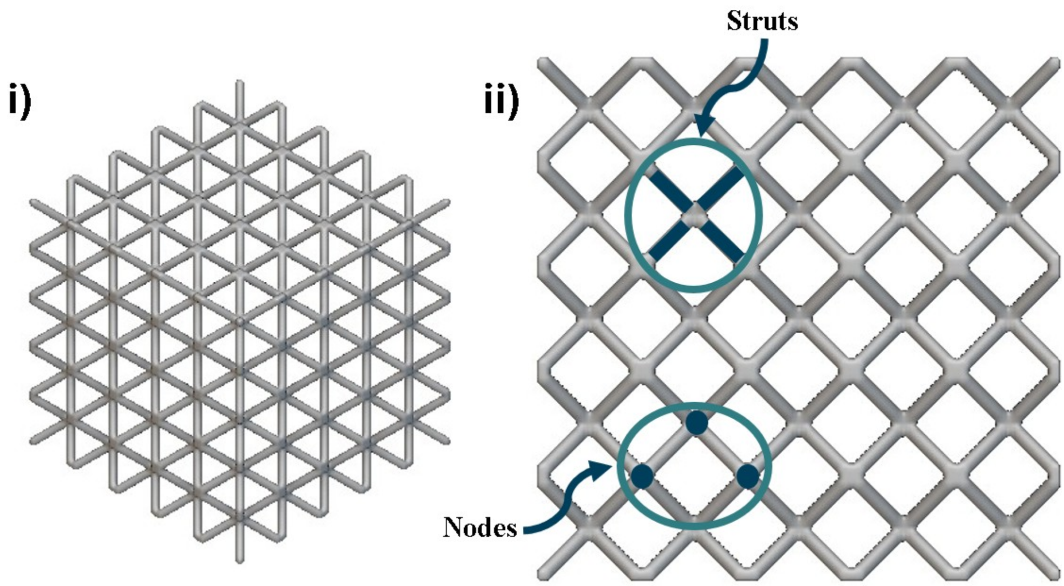

Figure 1.3: Figure (i) represents the complete Body Centered Cubic (BCC) Structure, while Figure (ii) highlights the struts and nodes that form the repeating unit-cell geometry.

The effective mechanical properties of a lattice structure can be adjusted by modifying several geometric parameters such as the strut diameter, **unit cell size**, **wall thickness**, and **the relative density** of the structure. These parameters directly influence the stiffness and deformation behavior of architected lattice materials.

In general, the effective elastic modulus E^* of a lattice structure is related to the relative density ρ^*/ρ_s of the structure through a power-law relationship given by:

$$E^* = C \left(\frac{\rho^*}{\rho_s} \right)^n E_s \tag{1.1}$$

where E_s is the elastic modulus of the solid material, ρ_s is the density of the solid material, and C and n are constants that depend on the lattice topology. This relationship allows designers to predict the mechanical response of the components.

As shown in figure 1.4, commonly used strut-based lattice architectures, including (i) Body Centered Cubic (BCC), (ii) Diamond, (iii) Face Centered Cubic (FCC),

(iv) Hexagonal Honeycomb, (v) Kelvin Cell, and (vi) Square Honeycomb structures. These lattice geometries are widely utilized in lightweight structural systems, energy absorption applications, and mechanically optimized designs due to their high stiffness-to-weight ratio and controllable deformation behavior.

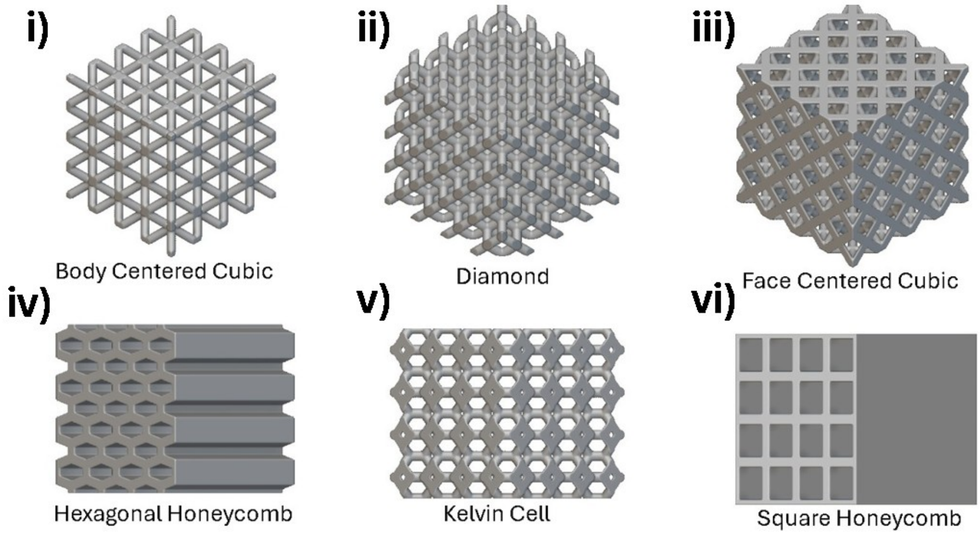

Figure 1.4: Examples of commonly used strut-based lattice architectures: (i) Body Centered Cubic (BCC), (ii) Diamond, (iii) Face Centered Cubic (FCC), (iv) Hexagonal Honeycomb, (v) Kelvin Cell, and (vi) Square Honeycomb structures.

As shown previously in Figure 1.3, these lattice architectures are composed of interconnected struts and nodes that collectively distribute mechanical loads throughout the structure. The struts function as the primary load-bearing members, while the nodes act as the connection points between multiple struts within the repeating unit-cell geometry.

Despite these advantages, strut-based lattice structures exhibit several limitations. The presence of discrete joints and sharp intersections between the struts often produces localized stress concentrations under compression, bending, or cyclic loading conditions. These stress concentrations can lead to premature buckling, fatigue damage, and crack initiation, particularly in applications involving repeated deformation and actuation.

Such failure mechanisms reduce the long-term reliability of soft robotic devices and limit the suitability of traditional lattice designs for highly deformable applications.

Figure 1.5 illustrates the basic gyroid block geometry used to represent the triply periodic minimal surfaces (TPMS) structure considered in this study.

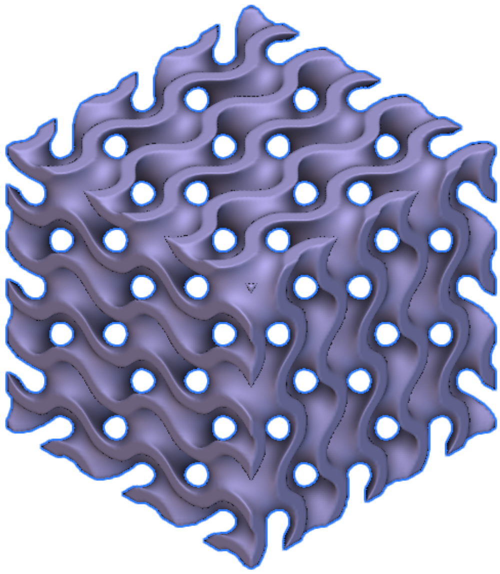

Figure 1.5: Gyroid block with a volume of $2\,\mathrm{mm}^3$, designed using nTop software (nTopology Inc., New York, USA).

The gyroid geometry can be described mathematically using an implicit surface equation given by:

$$\sin(x)\cos(y) + \sin(y)\cos(z) + \sin(z)\cos(x) = 0 \tag{1.2}$$

In practical designs, this equation is modified using an offset parameter to control the thickness or relative density of the structure, allowing mechanical properties to be tuned through geometry. Due to its continuous network throughout the sample, the gyroid structure also supports consistent fluid flow and uniform pressure distribution, which is beneficial for pneumatic soft robotic actuation and pressure sensing. For these reasons, gyroid architectures are selected in this work for soft robotic applications.

Among various lattice geometries, the gyroid structure is widely used due to its balanced mechanical performance and smooth continuous geometry. Unlike conventional strut-based lattice structures, the gyroid does not contain discrete joints or sharp connections.

This continuous surface enables a more uniform distribution of stress under mechanical loading, which reduces stress concentrations and delays the onset of buckling, fatigue, and crack propagation. Such characteristics are particularly important for soft robotic systems that undergo repeated deformation during operation.

The mechanical behavior of a soft robotic system is strongly influenced by its structural design architecture. Unlike rigid robotic systems, where stiffness is mainly determined by the material itself, soft robotic structures undergo a large deformation due to their compliant material properties. Instead, their deformation behavior is governed by the interaction between the compliant material properties and the geometry of the internal structure.

One of the most important mechanical characteristics in soft robotic systems is compliance, which refers to the ability of a structure to deform under applied loads. High compliance allows soft robots to safely interact with delicate objects and adapt to complex environments. However, excessive compliance can reduce structural stability. Therefore, soft robotic architectures must balance flexibility with sufficient stiffness to maintain controlled motion.

To achieve this balance, researchers have explored the use of engineered lattice structures and TPMS architectures, such as gyroid structures. These architectures allow the mechanical response of a structure to be tuned by modifying geometric parameters such as **wall thickness**, **edge length**, **relative density**, **unit cell**

size, and the overall topology of the lattice. By adjusting these parameters, it is possible to obtain a wide range of stiffness and deformation behaviours without altering the base material itself.

For example, Baker et al. (2023) [30] investigated elastomeric TPMS gyroid lattices in their study and demonstrated that structural geometry can significantly influence stiffness. The results showed that the elastic modulus of gyroid architectures varied from approximately 7.7 kPa to 293.4 kPa depending on the volume fraction and topology of the structure, indicating that the mechanical response can change by more than an order of magnitude through architectural modification alone.

Another important factor influencing the mechanical performance of lattice structures is **relative density**. Relative density describes the amount of solid material present in the structure compared with the total volume of the lattice. In general, increasing the relative density increases stiffness and load-bearing capacity, while decreasing the relative density increases porosity, flexibility, and deformability.

For gyroid structures, the mechanical response can be adjusted by changing the wall thickness and the amount of solid material within the unit cell. A low relative density produces a more open structure with thinner walls, whereas a high relative density produces a denser structure with thicker walls.

Figure 1.6 compares gyroid structures with relative densities of 20% and 60%. The 20% structure has a more porous architecture, which allows greater elastic deformation and is more suitable for soft robotic sensing applications. In contrast, the 60% structure contains more solid material, resulting in lower porosity and higher stiffness.

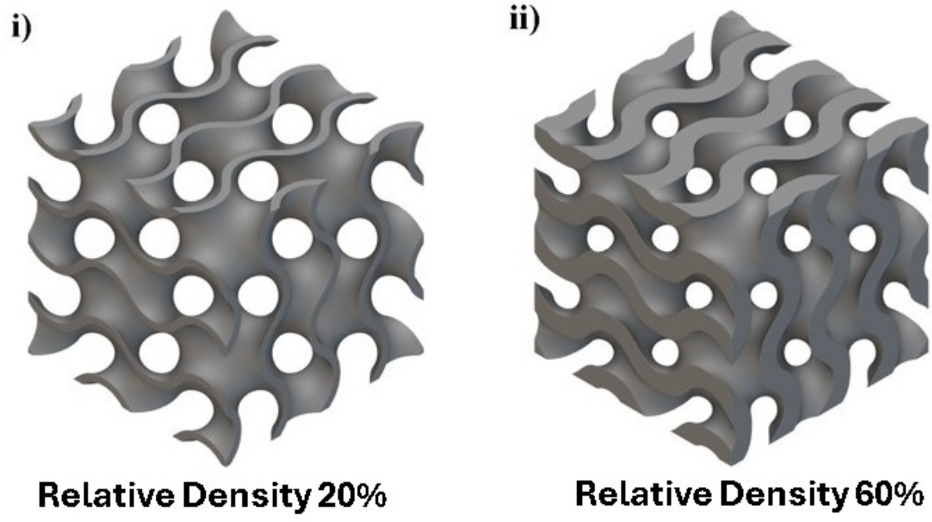

Figure 1.6: Comparison of gyroid structures with low and high relative density: (i) 20% relative density and (ii) 60% relative density.

Young's modulus is a mechanical property that describes the stiffness of a material, indicating how much it deforms under an applied load. In soft robotic systems, controlling stiffness is important because it directly affects flexibility, load-bearing capability, sensing response, and deformation behavior. The results demonstrated a strong relationship between structural density and mechanical stiffness, showing that gyroid architectures can be mechanically tailored for different soft sensing applications.

In the study by Kim et al. (2023) [31], the gyroid structures were fabricated from thermoplastic polyurethane (TPU) demonstrated that the Young's modulus could be tuned from 0.32 MPa at 30% relative density to 3.61 MPa at 80% relative density. TPU is a flexible and elastomeric polymer that combines rubber-like elasticity with good mechanical strength, making it suitable for 3D-printed soft robotic and sensing structures.

1.1.4 Material Behaviour of Soft Robots

Although structural architecture strongly influences mechanical behavior, the base materials used in soft robotics also play a crucial role in determining the overall performance of the system. Soft robotic structures are typically fabricated from elastomeric or rubber-like materials that can sustain large deformations while maintaining structural integrity.

Common materials used in soft robotic architectures include silicone elastomers, TPU, polydimethylsiloxane (PDMS), platinum-cured silicones, and flexible photopolymer resins. These materials are widely used because they exhibit high elasticity, low stiffness, and large strain capacity, allowing them to undergo bending, stretching, twisting, and compression without permanent deformation.

PDMS is commonly used in soft robotic systems because of its flexibility, biocompatibility, optical transparency, and ease of fabrication through molding and casting processes. It is widely utilized in soft microfluidic devices, pneumatic channels, and deformable sensing components. Platinum-cured silicones are frequently used for soft pneumatic actuators and wearable robotic systems due to their high elongation capability, durability, and stable mechanical behavior under repeated deformation and cyclic loading.

TPU is used in additively manufactured soft structures because of its flexibility with comparatively higher mechanical strength and abrasion resistance, making it suitable for 3D-printed lattice architectures and wearable robotic components. Flexible photopolymer resins are primarily used in resin-based additive manufacturing processes, where they enable the fabrication of geometrically complex soft structures with high dimensional accuracy and fine structural resolution.

A key mechanical characteristic of soft robotic materials is hyperelastic behavior, meaning that their stress–strain relationship is nonlinear and capable of supporting very large reversible deformations. Unlike conventional linear elastic materials, hyperelastic materials do not exhibit a constant stiffness throughout deformation. Instead, their mechanical response changes continuously as strain increases, allowing the material to undergo significant stretching, bending, and compression while returning to its original shape after unloading.

Figure 1.7 illustrates the typical nonlinear stress–strain behavior of a hyperelastic material. Initially, the material exhibits a compliant low-stiffness response where relatively large deformation occurs under small applied stress. As the strain increases, the material enters a nonlinear elastic region in which the stiffness changes continuously with deformation. At higher strain levels, the curve rises sharply due to strain stiffening behavior, where the material increasingly resists further deformation. This characteristic is important in soft robotic systems because it enables flexible motion while maintaining structural stability under large deformation.

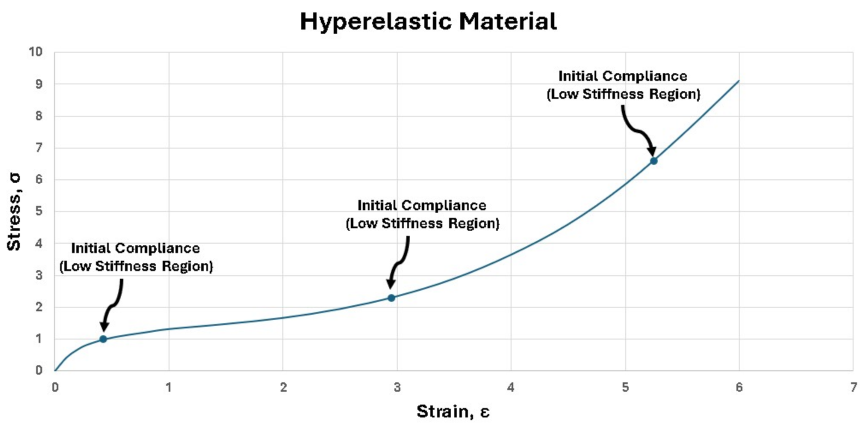

Figure 1.7: Stress–Strain response of a hyperelastic material showing high flexibility at low strain levels, nonlinear elastic deformation, and strain stiffening behavior at higher deformation levels. Graph is modified from [32].

In the elastomeric gyroid study by Baker et al. (2023) [30], mentioned earlier, silicone urethane elastomer materials were used to fabricate TPMS lattice structures using AM techniques. The combination of elastomeric material behaviour and architectural geometry enabled the structures to sustain large deformation while maintaining mechanical stability and recoverability after unloading.

Another important material property in soft robotics is fatigue resistance under cyclic loading. Soft robotic systems often operate through repeated actuation cycles, such as pneumatic inflation and deflation. Materials must therefore maintain mechanical integrity over many loading cycles. Experimental investigations on soft lattice structures have shown that structural dimensions such as strut thickness can significantly affect durability, with thinner structural elements showing earlier fatigue failure during repeated loading cycles [33].

Advances in 3D printing technologies allow complex architectures such as lattice networks and TPMS structures to be fabricated directly from soft materials. For example, TPU can be processed using fused deposition modeling (FDM) to produce porous gyroid structures with controlled mechanical properties. In some cases, foaming TPU materials can introduce internal porosity that further reduces stiffness and enhances sensing performance [31].

1.1.5 Sensing in Soft Robotic Systems

Sensing is an important requirement in soft robotic systems because soft robots must interact with objects, humans, and unstructured environments while maintaining their compliant behaviour. Unlike rigid robots, soft robots undergo large deformation during actuation and contact. Therefore, sensors used in soft robots must be flexible, stretchable, and mechanically compatible with the soft body. If the sensing element is too stiff or poorly integrated, it can restrict deformation and reduce the performance of the soft robotic structure.

Several sensing approaches have been developed for soft robots, including resistive, capacitive, optical, flexible electronic, fabric-based, and pneumatic sensors. Resistive sensors detect deformation through changes in electrical resistance. They are widely used because of their simple working principle and relatively easy integration into soft materials. However, they can suffer from hysteresis, signal drift, and durability issues during repeated deformation [34], [35].

Capacitive sensors measure deformation through changes in capacitance between conductive layers. These sensors can provide high sensitivity and are suitable for detecting pressure, strain, and contact. However, their performance can be affected by fabrication complexity, environmental noise, and changes in the dielectric material during large deformation [36], [37].

Optical sensors are another approach used in soft robotics. These sensors detect deformation by measuring changes in light transmission, reflection, or optical path length. They can be useful for strain and curvature sensing, but they often require careful alignment, optical fibers, or additional light-based components, which can make integration more complex [38], [39].

Flexible electronic sensors and strain-sensitive fabrics have also been used in soft robotic and wearable systems. These sensors can conform to curved and deformable surfaces, making them suitable for applications involving body motion, soft actuation, and contact detection. However, they may introduce wiring complexity, attachment challenges, and reduced repeatability under cyclic loading [40], [41].

Pneumatic sensing provides an alternative approach that is well suited to soft robotic systems. In pneumatic sensors, deformation or contact is detected through pressure changes inside internal chambers, channels, or air pathways. Since the sensing mechanism is based on pressure variation, pneumatic sensors can remain mechanically compliant and can be integrated into soft pneumatic structures without adding rigid sensing elements directly into the deformable body [13].

For example, Yang et al. [42] developed a pneumatic soft sensor for measuring contact force and curvature in a soft robotic gripper. The sensor used pressure changes inside a silicone-based sensing structure to estimate mechanical interaction during deformation. Pneumatic strain gauge concepts have also been investigated, where bending, stretching, or compression changes the geometry of internal air channels and produces measurable pressure variations [13], [42]–[44].

Although pneumatic sensing is mechanically compatible with soft robots, many existing pneumatic sensors mainly measure global deformation, bending, or strain. This means that the sensing output often represents the overall deformation of the structure rather than the exact location of contact. For soft pneumatic grippers, this is a limitation because contact can occur at different positions on the gripper or palm surface. Therefore, sensing methods that can provide localized pressure information while preserving softness and compliance are still needed.

1.2 Research Problem and Research Gap

Soft pneumatic grippers require sensing mechanisms that can detect contact and pressure while maintaining the compliance of the soft structure. Existing soft sensing methods can measure deformation, strain, curvature, or contact force, but their integration into highly deformable soft grippers remains challenging. Electrical, optical, and fabric-based sensors often require embedded conductive layers, electrodes, optical fibers, or wiring, which can increase fabrication complexity and may restrict the natural deformation of the soft body.

Pneumatic sensing is a promising alternative because it can detect mechanical interaction through pressure changes inside soft chambers or channels. This makes it more compatible with soft pneumatic systems compared with many rigid or semi-rigid sensing elements. However, many existing pneumatic sensing approaches mainly measure global deformation or strain. Some of the sensors can be affected by air leakage and ballooning of the soft chamber, which may reduce measurement stability [33], [42]. Leakage can lower the measured pressure response, while ballooning can cause unwanted structural expansion instead of localized deformation sensing [33].

This limitation is important for soft robotic manipulation. During grasping, the object may contact the gripper at different locations, especially in the palm region where contact forces can vary depending on object shape, position, and loading condition. A sensing system that only captures global deformation may not provide enough information about where pressure is applied or how the contact is distributed.

Therefore, the research gap addressed in this work is the need for a soft, structurally integrated pneumatic sensing architecture that can detect localized pressure changes while preserving the compliance of the gripper. This work investigates a gyroid as internal architecture as a deformable sensing structure for a soft pneumatic sensor. The aim is to evaluate whether the gyroid structure can generate measurable pressure variations under different applied weights and loading positions, providing a basis for localized tactile sensing in soft robotic applications.

1.3 Research Questions and Objectives

The goal of this thesis is to answer following research questions:

1. How can gyroid-based TPMS architectures be designed and fabricated as internal structures for soft pneumatic sensing applications?
2. How does the integration of a gyroid structure influence the pressure response of a pneumatic sensing system under localized touchpoint loading?
3. How can finite element simulation be used to evaluate the deformation behaviour of gyroid structures under loading?
4. How does gyroid cell size influence the measured pressure response and distributed sensing behaviour of the pneumatic sensor?

The primary aim of this thesis is to investigate the feasibility of gyroid structures as functional architectures for pneumatic tactile sensing in soft robotic systems. The study focuses on understanding how the integration of a gyroid structure within a confined sensing region influences pressure distribution and enables the detection of localized deformation through pressure variations.

To achieve this aim, the following objectives are defined:

- **Design Structures:** Evaluate various lattice and hybrid lattice structures by analyzing different geometric configurations.
- **Fabricate Structures:** Use additive manufacturing (AM) to 3D print lattice structures with soft materials.
- **Experimental Mechanical Characterization:** Perform tensile testing to experimentally characterize the mechanical behaviour of the fabricated structures.
- **Perform Structural Analysis:** Conduct finite element (FE) simulations to derive material properties from experimental data, followed by structural analysis of the lattice structures to validate deformation and load-response behaviour against experimental results.
- **Develop Soft Pneumatic Sensors:** Integrate the fabricated lattice structures into sensing components to design pressure sensors and evaluate their response under applied loading conditions.
- **Conduct an Experimental Evaluation:** Conduct experiments by applying controlled touchpoint interactions at different locations along the sensing region to generate pressure disturbances.
- **Identify Limitations and Improvements:** Examine system limitations such as air leakage and variability in response, and propose potential improvements.
- **Develop Comparative Control Samples:** Fabricate and evaluate empty-channel and sponge-based control structures to compare their sensing perfor-

mance against gyroid architectures.

1.4 Scope and Limitations

This thesis focuses on designing functional architectures for soft robotics. The study examines these architectures pressure-sensing elements for soft robotic applications. Sensor design, part 3D printing, and material testing are performed using elastomeric materials within the faculty setups. The first generation of sensors employs air as the working medium, where compressibility and the influence of different internal structures are examined. The second generation will further explore sensing mechanisms to investigate potential improvements in the overall sensor model.

FE simulations are focused on evaluating the mechanical behaviour and deformation response of the gyroid lattice structures under tensile loading conditions. The sensing capability of the pressure sensor architectures is evaluated experimentally through comparative demonstrations using gyroid, sponge-based, and empty-channel control structures.

The scope of this work is limited to structural and sensing evaluation under controlled laboratory conditions and does not include complete integration of the robotic system, implementation of closed-loop control, or long-term operational use.

1.5 Significance of the Work

This work contributes to the development of pneumatic sensing systems in soft robotics by exploring the use of a gyroid structure as an internal sensing element. Unlike conventional approaches that rely on single-point measurements, the proposed setup investigates how pressure variations can be captured at multiple locations within a continuous pneumatic network.

- **Spatial Pressure Variation:** Investigates pressure changes at different sensor locations to study how deformation propagates through the structure.
- **Response to Localized Interaction:** Examines whether different touch-point inputs can be distinguished based on pressure magnitude and timing.
- **Mechanically Driven Sensing:** Uses structural deformation and airflow variation as the sensing mechanism, reducing the need for embedded electronics within the sensing region.
- **Practical Implementation:** Demonstrates a sensing approach based on accessible components such as pressure sensors, tubing, and fabricated gyroid structures.
- **Role of Structural Design:** Highlights the potential of internal architecture as a design parameter for tuning the pressure response in future soft sensing applications.

1.6 Declaration on the Use of Generative AI

I declare that Generative AI was used only for language refinement, including grammar and sentence clarity. All research design, experimentation, analysis, and results are entirely my own work.

1.7 Outline of the Thesis

The thesis is divided into seven chapters.

Chapter 1 introduces the background of soft robotics, architected soft structures, and pressure sensing systems together with the research motivation, objectives, scope, and research questions of the study.

Chapter 2 presents the methodology used throughout the work, including the research workflow, materials, computational tools, AM process, and experimental approach used for both the mechanical and sensing investigations.

Chapter 3 focuses on the design and Finite Element modelling of the gyroid structures. The development of the lattice geometries, hyperelastic material modelling, and simulation setup used for evaluating the mechanical behaviour of the structures are discussed in this chapter.

Chapter 4 presents the fabrication and experimental testing of the developed gyroid samples. The chapter includes the SLA printing process, specimen preparation, tensile testing setup, and experimental procedures used during the mechanical characterization.

Chapter 5 presents the numerical and experimental results together with the comparison between simulation and experimental observations. The accuracy of the developed FE models and the mechanical response of the gyroid structures are discussed.

Chapter 6 introduces the comparative pressure sensor demonstration developed using different internal architectures, including empty, sponge-based, and gyroid structures. The sensing response and overall behaviour of the different sensor configurations are experimentally compared.

Finally, Chapter 7 summarizes the main findings of the thesis, discusses the limitations of the current work, and presents recommendations for future research.

2 Methodology

2.1 Research Approach

The quantitative component of this research focuses on the experimental characterization of the material and numerical simulation of the designed gyroid structures.

Since the soft material used for the sensor architecture did not initially have defined mechanical parameters required for numerical simulation, experimental testing was first conducted to determine its mechanical behavior. A uniaxial tensile test was performed on material specimens to obtain the stress–strain response of the material.

The experimental data obtained from the tensile tests were used to determine a suitable hyperelastic material model. Hyperelastic models are commonly used to describe the nonlinear deformation behavior of elastomeric materials used in soft robotic systems. The stress–strain data obtained from the experiments were fitted to different hyperelastic constitutive models in Abaqus (Dassault Systèmes Simulia Corp., Providence, Rhode Island, USA), allowing the identification of the model that best represented the mechanical behavior of the material.

Once the hyperelastic parameters were determined, the gyroid structures generated in nTop (nTopology Inc., New York, USA) were exported as mesh geometries and imported into Abaqus/CAE for numerical simulation. Finite element simulations were then performed to evaluate the structural response of the gyroid lattice under loading conditions.

To evaluate the accuracy of the numerical model, the simulation results were compared with the experimental observations. This comparison was used to assess how well the selected hyperelastic material model and simulation setup represented the real mechanical behavior of the printed gyroid structure.

After validating the simulation model, the obtained numerical results were used to guide the development of the proof-of-concept structures and final sensor architecture. This quantitative approach enabled the evaluation and optimization of the gyroid-based structures for soft robotic sensing applications.

2.2 Overall Research Workflow

The research methodology followed in this study included design, fabrication, mechanical characterization, simulation, and sensing demonstration stages in sequence. The workflow first focused on the development and mechanical validation of gyroid lattice structures, followed by their use in a proof-of-concept pneumatic sensing system. This ensured that the sensing experiments were supported by prior understanding of the material response and structural behaviour of the gyroid samples.

AM was used as the fabrication method because it enables complex gyroid geometries to be produced directly from digital models. The experimental and simulation stages were then combined to evaluate whether the designed gyroid structures could be mechanically characterized and later applied as internal sensing architectures. The overall workflow also provides a clear link between design, material testing, FE modelling, mechanical validation, and the final sensor comparison.

Figure 2.1 illustrates the overall research workflow followed in this study. The process begins with gyroid design in nTop, followed by SLA-based AM fabrication using elastomeric resin materials. The printed specimens are then mechanically characterized, and the experimental data are used for hyperelastic material modelling and FE simulation in Abaqus. The simulation results are compared with experimental testing to validate the numerical model. After validation, the gyroid structures are integrated into the pneumatic sensor setup and compared with empty-channel and sponge-based configurations for pressure sensing evaluation.

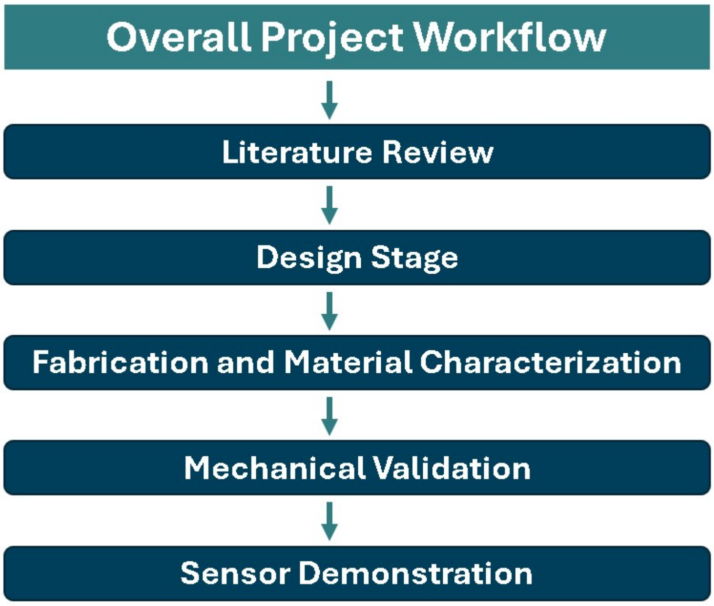

Figure 2.1: Overall research workflow showing the sequence from gyroid design and AM fabrication to material characterization, FE simulation, experimental validation, and comparative pressure sensor demonstration.

2.3 Materials, Tools, and Methods Overview

This study combines computational modelling, AM fabrication, and experimental testing to evaluate gyroid-based soft robotic structures. Flexible 80A Resin and Silicone 40A Resin, supplied by Formlabs Inc. (Somerville, Massachusetts, USA), were used to fabricate the lattice specimens using SLA-based AM. The gyroid geometries were designed in nTop, while FE simulations were performed in Abaqus to evaluate the nonlinear mechanical behaviour of the structures under large deformation conditions.

Experimental characterization was conducted using tensile testing to obtain the material response required for hyperelastic constitutive modelling and simulation calibration. The tensile tests were performed using a TA.XTplus Texture Analyser by Stable Micro Systems Ltd. (Godalming, UK). In addition to the mechanical investigations, comparative pressure sensor demonstrations were performed using different internal structural configurations to evaluate their sensing response under applied loading conditions.

Table 2.1 summarizes the principal materials, computational tools, manufacturing methods, and experimental techniques used throughout this study.

Table 2.1: Overview of the main materials, computational tools, and experimental methods used in this study.

Category	**Tool / Material**	**Purpose**
Material	Flexible 80A Resin (Formlabs Inc., USA)	Fabrication of elastomeric gyroid structures
Material	Silicone 40A Resin (Formlabs Inc., USA)	Fabrication of highly compliant soft sensing structures
Design software	nTopology (nTop, nTopology Inc., USA)	Implicit modelling and gyroid lattice generation
Simulation software	Abaqus (Dassault Systèmes, France)	Finite element analysis and hyperelastic material modelling
Manufacturing method	SLA additive manufacturing	Fabrication of high-resolution lattice structures
3D printer	Formlabs Form 3+ (Formlabs Inc., USA)	Printing of elastomeric samples and sensor structures
Experimental testing	TA.XTplus Texture Analyser (Stable Micro Systems Ltd., UK)	Tensile characterization and mechanical testing

3 Design and Simulation of Gyroid Structures

3.1 Selection of the Gyroid TPMS Architecture

The design architecture plays a critical role in determining the mechanical behavior, compliance, deformation response, and sensing capability of soft robotic structures. Architected cellular geometries enable the mechanical properties of a structure to be tailored through controllable design parameters such as unit cell top, relative density, wall thickness, and volume fraction [45]. Unlike conventional solid materials, architected lattice structures derive a significant portion of their mechanical behavior from geometry rather than material composition alone. As a result, the same base material can exhibit substantially different stiffness, energy absorption capability, compressibility, and deformation characteristics depending on the selected structural architecture.

Al-Ketan et al. (2019) [45] demonstrated that TPMS lattices can provide highly tunable mechanical performance while maintaining lightweight and continuous structural characteristics. Their work showed that geometrical parameters strongly influence the effective elastic modulus, stress distribution, and deformation behavior of the lattice structures. These properties are particularly important in soft robotics, where compliant deformation, controlled stiffness, and distributed load transfer are essential for achieving safe interaction and adaptive mechanical functionality.

Among various architected lattice structures, TPMS geometries have gained significant attention due to their smooth and continuous surfaces, high surface-to-volume ratio, and favorable mechanical performance. TPMS structures divide space into multiple interconnected regions while maintaining zero mean curvature across the surface. This continuous topology provides improved stress distribution and structural stability compared to traditional strut architectures. [46]

One of the most widely studied TPMS structures is the gyroid architecture, first identified by Alan Schoen in 1970. The gyroid structure can be mathematically described using sinusoidal equations that generate a continuous periodic surface throughout three-dimensional space. By modifying parameters in these mathematical expressions, the mechanical properties of the gyroid structure can be tuned for specific applications. [47]

Compared with conventional lattice structures, gyroid architectures provide several advantages, including:

- Smooth and continuous surfaces without sharp geometric intersections
- More uniform stress distribution throughout the structure
- High surface-to-volume ratio due to the interconnected porous geometry
- Tunable mechanical stiffness and structural compliance through geometric parameter variation

Figure 3.1 shows the geometry used for the surface-area and volume-fraction comparison. Figure 3.1(i) illustrates the generated gyroid lattice structure, while Figure 3.1(ii) shows the equivalent rectangular bounding block used as the reference solid geometry.

Additionally, the gyroid topology enables precise control of mechanical properties through structural parameters such as volume fraction and relative density. Gyroid lattice structures reduce the amount of solid material while maintaining a continuous internal geometry.

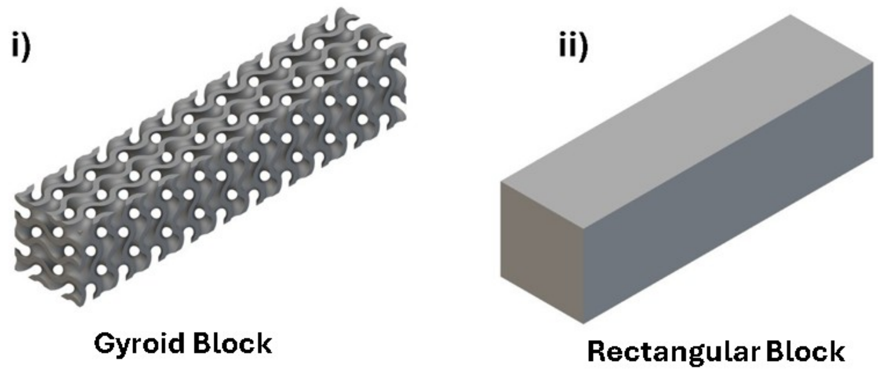

Figure 3.1: Gyroid structure used for geometric analysis and volume fraction calculation.

The comparison between the gyroid structure and the solid block was used to evaluate how the gyroid architecture reduces material volume while maintaining a high surface area. The main design and analysis parameters used for this geometric comparison are summarized in Table 3.1.

Table 3.1: Design parameters used for the gyroid structure.

Parameter	**Value**	**Description**
Bounding Block Dimensions	$50 \times 10 \times 10$ mm	External dimensions of the reference block
Gyroid Unit Cell Size	5 mm	Repeating unit cell dimension
Wall Thickness	0.95 mm	Thickness of the gyroid sheet structure
Boolean Operation	Intersect	Gyroid structure trimmed using the bounding block
Relative Precision	0.01	Tolerance used during geometric evaluation
Block Volume	5000 mm^3	Volume of the equivalent solid block
Gyroid Material Volume	1947.01 mm^3	Material volume of the gyroid structure
Volume Fraction	0.389	Ratio of gyroid material volume to block volume
Gyroid Surface Area	6458.81 mm^2	Surface area of the gyroid structure
Block Surface Area	2197.06 mm^2	Surface area of the equivalent solid block

The bounding block used for comparison has dimensions of $50 \times 10 \times 10$ mm. Therefore, the external volume of the reference block is

$$V_{\text{block}} = 50 \times 10 \times 10 = 5000 \text{ mm}^3 \tag{3.1}$$

The volume fraction is defined as the ratio between the material volume of the gyroid structure and the volume of the equivalent solid block:

$$\phi = \frac{V_{\text{gyroid}}}{V_{\text{block}}} \tag{3.2}$$

For the gyroid model considered in this study, the material volume is approximately

$$V_{\text{gyroid}} \approx 1947.01 \text{ mm}^3 \tag{3.3}$$

which gives a volume fraction of

$$\phi = \frac{1947.01}{5000} \approx 0.389 \tag{3.4}$$

As shown in Figure 3.1 and summarized in Table 3.1, the gyroid structure has a larger surface area than the equivalent solid block while using only a fraction of the total block volume. The surface area comparison can be expressed as

$$A_{\text{gyroid}} \approx 6458.81 \text{ mm}^2 \quad > \quad A_{\text{block}} \approx 2197.06 \text{ mm}^2 \tag{3.5}$$

This indicates that the gyroid architecture provides a high surface-area-to-volume relationship while maintaining a reduced material volume. Such behaviour is useful for lightweight structures and applications where increased surface interaction, deformation capability, or fluid interaction is required.

Due to these advantages, gyroid structures can be used for applications including pressure sensing [31], energy absorption systems [31], biomedical scaffolds, [31] and soft robotic architectures [30], [33]. In soft robotic systems, architected lattice structures are particularly attractive because they enable lightweight, compliant, and mechanically tunable designs while maintaining structural flexibility and distributed deformation capability [21], [48].

3.2 Gyroid Sample Design

To design the gyroid architecture used in this study, multiple computational tools were initially explored for generating the lattice structures. The objective of this exploration was to identify a design platform capable of efficiently generating complex TPMS geometries while allowing flexible control of structural parameters.

During the design stage, several software tools were evaluated for the generation of gyroid and other lattice structures. Each platform provides different capabilities for parametric modelling, scripting, and lattice generation. The following tools were considered during the initial design exploration:

As shown in Figure 3.2, the structures generated using (i) *OpenSCAD*, (ii) *MATLAB*, (iii) *PTC Creo*, and (iv) *nTop* represent examples of gyroid and lattice-based geometries created using different computational design tools. These examples show that each tool provides different capabilities for generating gyroid and TPMS-based architectures used in soft robotic and lattice modelling workflows.

- *OpenSCAD* (OpenSCAD Project, open-source software, USA)
- *MATLAB* (MathWorks Inc., Natick, Massachusetts, USA)
- *PTC Creo* (PTC Inc., Boston, Massachusetts, USA)
- *nTop* (nTopology Inc., New York, New York, USA)

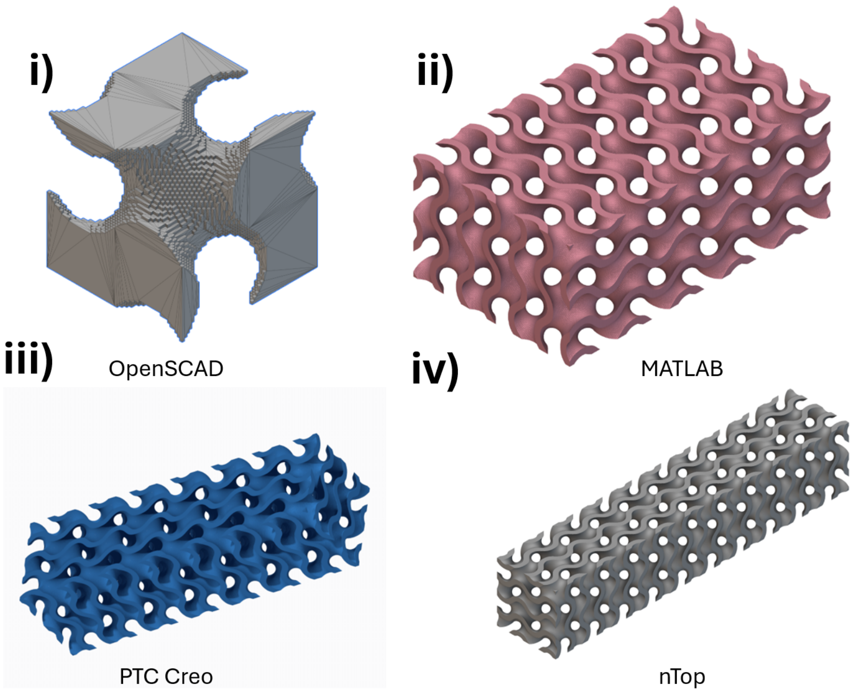

Figure 3.2: Examples of gyroid and lattice structures generated using different design tools: (i) *OpenSCAD*, (ii) *MATLAB*, (iii) *PTC Creo*, and (iv) *nTop*.

OpenSCAD and MATLAB provide flexibility for creating mathematically defined geometries through scripting and parametric modelling. In MATLAB, TPMS structures can be generated using implicit mathematical equations evaluated across a spatial grid. However, the resulting surfaces must typically be converted into mesh formats such as STL through additional processing steps. This conversion is required because mesh formats such as STL are widely used for 3D printing, FEA, and CAD-based manufacturing workflows.

Similarly, OpenSCAD allows parametric modelling and Python scripting, but generating complex TPMS surfaces often requires custom scripts and surface reconstruction, which increases modelling complexity and development time.

PTC Creo offers CAD modelling capabilities and is widely used for conventional mechanical design. However, traditional CAD systems are primarily based on boundary representation (B-rep) modelling, which relies on sketches, surfaces, and solid features. The term B-rep modeling means that the geometry is created by defining the outer surfaces, edges, and solid boundaries of an object rather than generating mathematically continuous internal structures directly. As a result, creating mathematically defined TPMS geometries such as gyroids can be challenging and often requires complex surface approximations or imported mesh geometries.

Among the evaluated tools, nTop provided the most efficient workflow for generating gyroid structures. The software uses implicit modelling and field-driven design methods, allowing complex lattice structures to be defined directly through mathematical fields rather than explicit surface modelling. This approach enables smooth geometry generation, improved control over lattice parameters, and efficient modification of structural properties such as unit cell size and thickness.

In addition, implicit modelling significantly reduces many of the geometric reconstruction issues commonly encountered in conventional CAD workflows when handling highly complex TPMS geometries. However, due to the mathematical evaluation of continuous fields and high geometric complexity, the computational requirements can become demanding for large-scale or high-resolution lattice structures, particularly during meshing, visualization, and export operations.

One advantage of nTop is the ability to modify gyroid structures using parametric design variables. Several parameters were adjusted during the design process to study their influence on the structural behavior.

Figure 3.3 illustrates the main geometric parameters considered in the gyroid lattice design. The unit cell shown in Figure 3.3(i) is periodically repeated to form the complete TPMS lattice structure, while Figure 3.3(ii) shows how decreasing wall thickness changes the lattice geometry.

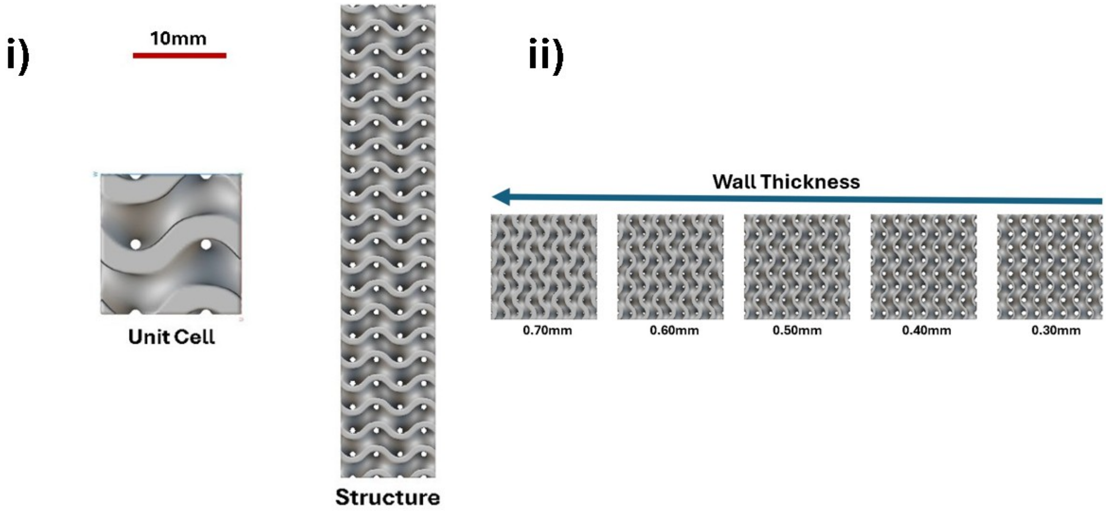

Figure 3.3: Gyroid lattice design parameters: (i) gyroid unit cell and its periodic repetition forming the complete structure, and (ii) wall thickness variation from 0.70 mm to 0.30 mm. Images were created in nTop.

Unit Cell Size: The unit cell size controls the periodic spacing of the gyroid lattice within the structure. Changing the unit cell size affects the density and mechanical response of the lattice. Smaller unit cells generally create denser structures with higher stiffness, while larger unit cells produce more compliant structures.

Wall Thickness: The wall thickness of the gyroid surface determines the relative density of the lattice structure. Increasing the wall thickness increases structural stiffness and load-bearing capability, while thinner walls produce more flexible structures suitable for soft robotic sensing applications. Therefore, wall thickness was treated as an important design parameter for controlling the mechanical response of the structure.

In this study, nTop was selected because its implicit modeling environment allows wall thickness, unit cell size, and spatial classification to be controlled directly using field-driven operations. Tools such as ramp and clamp functions allow gradual variation of structural parameters across the geometry, where properties such as wall thickness or cell size change progressively throughout the structure rather than remaining constant. This made nTop suitable for generating graded gyroid structures and smooth transitions between solid and lattice regions within the tensile specimen design.

3.3 Material Model Definition

Soft robotic systems are commonly fabricated using elastomeric materials that are capable of having large reversible deformations under applied loading. Unlike conventional engineering materials that exhibit approximately linear elastic behaviour at small strains, elastomeric materials demonstrate highly nonlinear stress–strain responses when subjected to tension, compression, or bending. These materials can sustain significant deformation while returning to their original shape after unloading, making them particularly suitable for compliant structures and soft robotic applications.

In FE simulations, the mechanical behaviour of hyperelastic materials cannot be accurately represented using conventional linear elastic models because elastomeric materials exhibit nonlinear stiffness during deformation. Instead, specialized hyperelastic constitutive formulations are required to describe the stress–strain relationship under large deformation conditions.

Several hyperelastic material models are commonly used in computational mechanics, including the Neo–Hookean model [49], the Mooney–Rivlin model [50], [51], the Ogden model [52], and the Yeoh model [53]. These formulations are based on strain energy density functions that approximate the nonlinear response of elastomeric materials using experimentally determined material constants.

The Neo–Hookean model is one of the simplest hyperelastic constitutive formulations and is commonly used for small to moderate deformation conditions. Its strain energy density function is expressed as

$$W = C_{10}(\bar{I}_1 - 3) \tag{3.6}$$

where W is the strain energy density function, C_{10} is a material parameter, and $\bar{I}_1$ is the first deviatoric strain invariant.

For improved representation of nonlinear behaviour at larger strains, the Mooney–Rivlin model introduces an additional strain invariant term and is written as

$$W = C_{10}(\bar{I}_1 - 3) + C_{01}(\bar{I}_2 - 3) \tag{3.7}$$

where C_{10} and C_{01} are experimentally fitted material constants, while $\bar{I}_1$ and $\bar{I}_2$ are the first and second strain invariants.

The Yeoh model extends the formulation using higher-order polynomial terms of the first strain invariant:

$$W = \sum_{i=1}^{3} C_{i0}(\bar{I}_1 - 3)^i \tag{3.8}$$

This model is widely used for silicone-based elastomers because it can accurately capture strain stiffening behaviour at large deformation levels.

The Ogden model represents the material response using principal stretch ratios and is particularly suitable for modelling highly nonlinear elastomeric deformation:

$$W = \sum_{i=1}^{N} \frac{\mu_i}{\alpha_i} (\lambda_1^{\alpha_i} + \lambda_2^{\alpha_i} + \lambda_3^{\alpha_i} - 3) \tag{3.9}$$

where μ_i and α_i are material constants, and λ_1, λ_2, and λ_3 represent the principal stretch ratios.

The selection of an appropriate constitutive model depends on the material type, deformation range, and the level of accuracy required for the simulation. In soft robotic applications, models such as Yeoh and Ogden are frequently preferred because they provide improved fitting for highly deformable elastomeric materials subjected to large strain conditions.

Abaqus provides multiple hyperelastic material formulations that can be calibrated directly using experimental test data. The software determines the constitutive parameters by fitting mathematical strain energy functions to experimentally measured stress–strain curves. To perform this fitting process reliably, accurate experimental material characterization is required.

For this reason, uniaxial tensile testing was conducted to obtain the mechanical response of the elastomeric materials used in this study. Tensile testing provides the nominal stress–strain behaviour required for defining hyperelastic constitutive models in finite element simulations. The experimentally obtained data were later used within Abaqus to calibrate and evaluate different hyperelastic material formulations.

In order to evaluate the mechanical behaviour of the gyroid lattice structures, standardized tensile specimen geometries were used. ASTM tensile testing standards are widely used because they define specimen dimensions, gauge lengths, gripping regions, and testing conditions required for accurate comparison of material properties such as tensile strength, elongation, and deformation behaviour. These tests were also performed by texture anayzer for mechanical characterization. For the Silicone 40A specimens, the specimen was designed according to the ASTM D412 Type C standard, the Flexible 80A resin specimens were designed using the ASTM D412 Type A geometry, which is commonly used for highly flexible elastomeric materials and rubber-like specimens.

The specimen geometry consisted of a central gauge region and two enlarged gripping sections used for mounting the specimen within the tensile testing device. The gyroid lattice was introduced within the central gauge region of the specimen, where the mechanical response of the structure was to be measured, similar to previously reported lattice characterization approaches in the literature [54].

The table 3.2 shows a comparison of properties between the 2 resins, flexible 80A and Silicone 40A from formlabs.

Table 3.2: Mechanical properties of selected Formlabs elastomeric resins.

Property	**Flexible 80A**	**Silicone 40A**
Shore Hardness	80A	40A
Elongation at Break	∼120%	∼230%
Tensile Strength	∼8.9 MPa	∼3.5 MPa
Material Behaviour	Semi-flexible	Highly compliant
Typical Application	Durable flexible parts	Soft robotic actuators and sensors
Printing Process	SLA Resin Printing	SLA Resin Printing

Figure 3.4 illustrates the concept of the designed specimen. Figure 3.4(i) shows the CAD of the tensile specimen, where the central gauge region containing the gyroid lattice is highlighted, while the gripping sections remain solid to support the clamping mechanism. Figure 3.4(ii) shows the fabricated specimens produced using Flexible 80A and Silicone 40A resins for comparison.

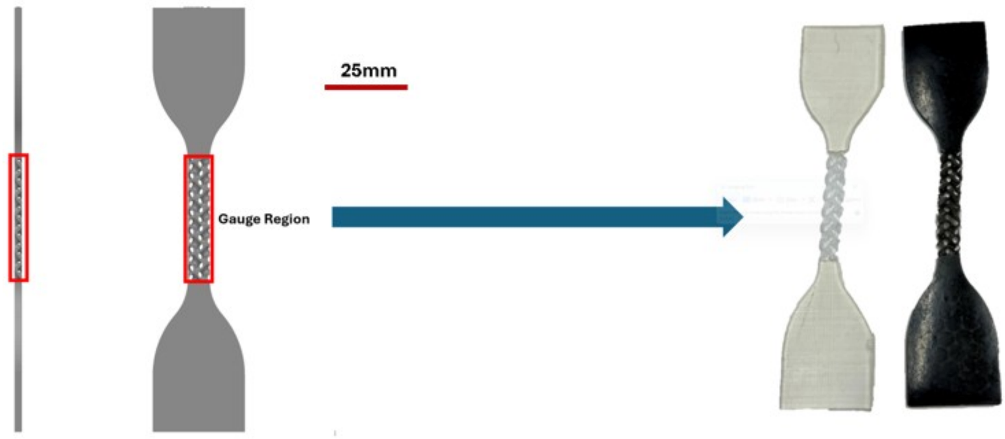

Figure 3.4: (i) CAD design of the gyroid tensile specimen showing the highlighted gauge region containing the lattice structure, and (ii) fabricated specimens produced using Flexible 80A and Silicone 40A resins.

3.4 FE Model of Gyroid Samples

3.4.1 Geometry Import

FE simulations were performed using the Abaqus simulation environment available through the Abaqus CAE research license provided by the university. The available license allows simulations of approximately 250 000 nodes.

Abaqus was selected because it provides reliable finite element tools for nonlinear structural analysis and advanced material modelling. The software supports both implicit and explicit solutions, allowing different types of mechanical problems to be simulated within the same environment. Implicit solution methods are commonly used for stable, quasi-static problems where the loading occurs gradually, while explicit solution methods are more suitable for highly nonlinear, dynamic, or complex contact problems involving large deformation and rapid structural response.

In this study, Abaqus solver was primarily used since it is well suited for quasi-static loading conditions and nonlinear material behaviour. Abaqus also provides robust material modelling capabilities and accurate contact formulations, which are commonly used in engineering simulations involving large deformation and elastomeric materials.

3.4.2 Material Model Identification

To determine suitable hyperelastic material parameters for the printed material, the experimental stress–strain data obtained from uniaxial tensile tests of **solid specimens** were used for material model calibration. These solid specimens were printed from the same material as the gyroid structures and were tested to characterize the base material behaviour independently from the geometric effects of the lattice architecture.

The process was carried out within the Abaqus material evaluation environment. In this workflow, the experimentally measured nominal stress–strain data from the solid tensile specimens were imported into the material definition module and assigned as uniaxial test data.

Within the Abaqus material modelling interface, a new material was created in the *Property* module. The hyperelastic behaviour was defined by selecting the *Mechanical* → *Elasticity* → *Hyperelastic* option. Abaqus provides several hyperelastic constitutive formulations that can be fitted to experimental test data, including Neo-Hookean, Mooney–Rivlin, Ogden, and Yeoh models.

These models are widely used to represent the nonlinear response of elastomeric materials under large deformation. The appropriate constitutive model was selected by fitting the experimentally obtained stress–strain data from the solid specimens to the available hyperelastic formulations and evaluating the accuracy of the material response prediction under tensile loading conditions. Among these models, the Mooney–Rivlin and Ogden formulations are commonly preferred for soft robotic elastomers because they provide improved accuracy in capturing nonlinear deformation behaviour over a wide strain range.

3.4.3 Meshing Generation

Before generating the numerical mesh for the specimen geometry, several meshing considerations were taken into account in order to obtain reliable results for the elastomeric materials. Since hyperelastic materials undergo large deformation and significant strain gradients during loading, the mesh resolution must be sufficient to capture the deformation behaviour accurately. In practice, the element size is usually related to the smallest geometric feature of the structure, particularly the wall thickness. A common guideline is to maintain approximately three to four finite elements across the minimum thickness of the structure. For example, if the minimum wall thickness is 1 mm, the element edge length should be approximately 0.25−0.33 mm. Using only a single element across the thickness can result in unrealistic bending behaviour and artificial stiffness in the numerical model.

In the present study, the geometry exported from the design stage was first represented using a triangular surface mesh, which defines the external geometry of the specimen. This surface discretization was then used to generate the tetrahedral volume mesh that defines the interior finite element model and carries the material behavior in the simulation.

The simulations were performed using the C3D10H element available in Abaqus. This element is a quadratic ten-node tetrahedral continuum element with a hybrid formulation. Hybrid elements are commonly used for materials with large deformations such as elastomers, since they reduce the numerical locking effects that may occur when modeling rubber-like materials with standard displacement-based elements. The snippet can be seen from the figure 3.5.

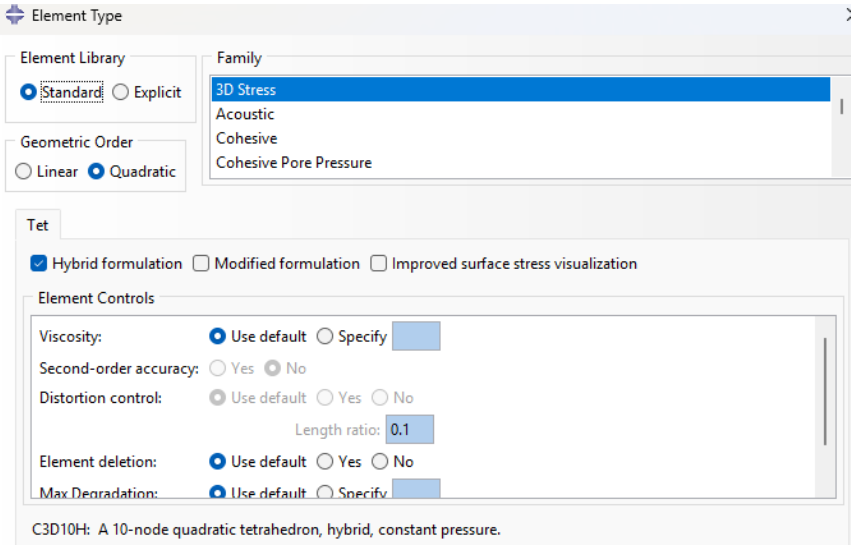

Figure 3.5: Element type configuration in Abaqus showing the C3D10H hybrid quadratic tetrahedral element used for the finite element simulations.

Although structured hexahedral meshes are often preferred in finite element analysis due to their numerical accuracy, generating high-quality hexahedral meshes for complex geometries such as gyroid structures is challenging. Hexahedral meshing typically requires sweepable regions and predictable topology, which are not present in TPMS-based geometries. For this reason, tetrahedral meshing was selected in this work, as it allows the complex geometry of the structure to be discretized more reliably while maintaining acceptable element quality for the numerical simulations.

After identifying the hyperelastic material parameters from the experimental stress–strain data, the next step involved preparing the specimen geometry for numerical simulation in Abaqus. The tensile specimen geometry generated during the design stage was exported from the design environment and imported into the FE model.

During the initial mesh generation stage, the exported specimen contained a large number of elements. The first mesh generated from the design model resulted in approximately 2.39 million elements, which exceeded the computational limitations of the available Abaqus research license. The HubX license used in this work allows simulations with a maximum limit of approximately 250 000 nodes, which required significant reduction of the mesh density before the geometry could be used for simulation.

Since the surface geometry exported from nTop was composed of triangular surface elements, each element contained three nodes. To remain within the node limit imposed by the software license, the total number of elements therefore needed to be kept below approximately 83 000 elements. This constraint required several adjustments to the mesh generation parameters within the design environment.

Figure 3.6 compares the initial fine mesh and the reduced mesh used for the finite element simulations. Figure 3.6(i) shows the initial high-resolution mesh generated from the exported gyroid geometry, which contained a larger number of elements and exceeded the practical computational limit. Figure 3.6(ii) shows the reduced mesh after adjusting the mesh export parameters, which allowed the model to remain within the Abaqus license limit while preserving the overall geometry of the specimen.

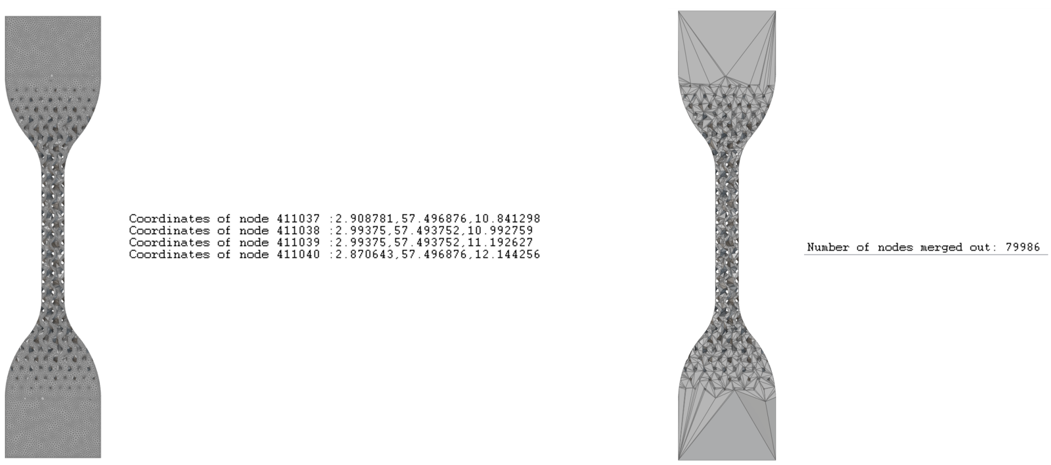

Figure 3.6: Comparison between the initial high-resolution mesh and the reduced mesh used for numerical simulations: (i) initial fine mesh and (ii) reduced mesh.

In order to reduce the mesh size, parameters such as edge length, feature size, and minimum edge length were modified during the mesh export process. Through iterative adjustments of these parameters, the mesh density was progressively reduced from the initial mesh size to approximately 300 000 elements, and finally to a mesh containing 79 896 elements. This configuration allowed the model to remain within the computational limits of the Abaqus license while maintaining a reasonable representation of the specimen geometry.

Although the resulting mesh was a coarse mesh compared to the original high-resolution geometry, it provided a practical balance between geometric accuracy and computational feasibility. The prepared mesh was then imported into Abaqus for the subsequent finite element simulations.

After preparing the lattice geometry and generating the computational mesh in nTop, the next step involved exporting the model for finite element analysis in Abaqus. Several export strategies were evaluated in order to obtain a simulation-ready model while maintaining compatibility with the available software tools and computational limitations.

The lattice model was exported from nTop in the `.inp` format for use in Abaqus. This format preserves the volumetric finite element mesh, including node coordinates and element connectivity, allowing the mesh to be directly imported without additional remeshing.

Alternative export formats such as `.stl` were also evaluated during the model preparation stage. However, STL files represent only the triangulated surface of a geometry and do not contain volumetric mesh information. Consequently, the model would require additional processing and remeshing in Abaqus before it could be used for finite element analysis. Since the tensile simulations in this study require volumetric continuum elements to accurately represent the deformation of the structure, the STL format was not considered suitable for the final simulation workflow.

Another strategy that was investigated involved importing the generated mesh into Abaqus and reconstructing a geometric model using the *Create Geometry from Mesh* plugin in Abaqus. In this approach, the imported model is first treated as an orphan mesh, after which Abaqus attempts to generate an approximate geometric representation from the mesh surfaces.

However, due to the very high mesh density of the lattice structure, the reconstructed geometry became challenging to manipulate and remesh within the Abaqus environment. As a result, editing operations and further mesh refinement needed computationally power and inefficient for the simulation workflow.

Based on these observations, the most practical solution was to directly import the `.inp` file generated from nTop and perform the simulations using the orphan mesh. During this process, certain mesh-related errors were occasionally encountered, such as warnings indicating the presence of unconnected regions in the model. These issues were resolved using the mesh editing tools available in Abaqus, particularly the *Edit Mesh* functionality, where nearby nodes were merged by adjusting the node tolerance. This ensured mesh continuity and allowed the finite element model to be successfully prepared for simulation.

3.4.4 Solver Setting

The .inp file of the tensile specimen was imported into Abaqus/CAE and treated as an orphan mesh. Since the imported model did not contain editable native geometry, the gripping regions were defined directly from the mesh. The upper and lower surfaces of the specimen were selected and defined as surfaces representing the upper and lower clamps. These surfaces were later used for applying boundary conditions and interactions during the tensile simulation.

Figure 3.7 shows the finite element model of the tensile specimen after import into Abaqus/CAE. The figure highlights the mesh distribution and the two boundary regions used to represent the tensile test clamps. The upper region was defined as the moving clamp, where displacement was applied during the simulation, while the lower region was defined as the fixed clamp to constrain the specimen.

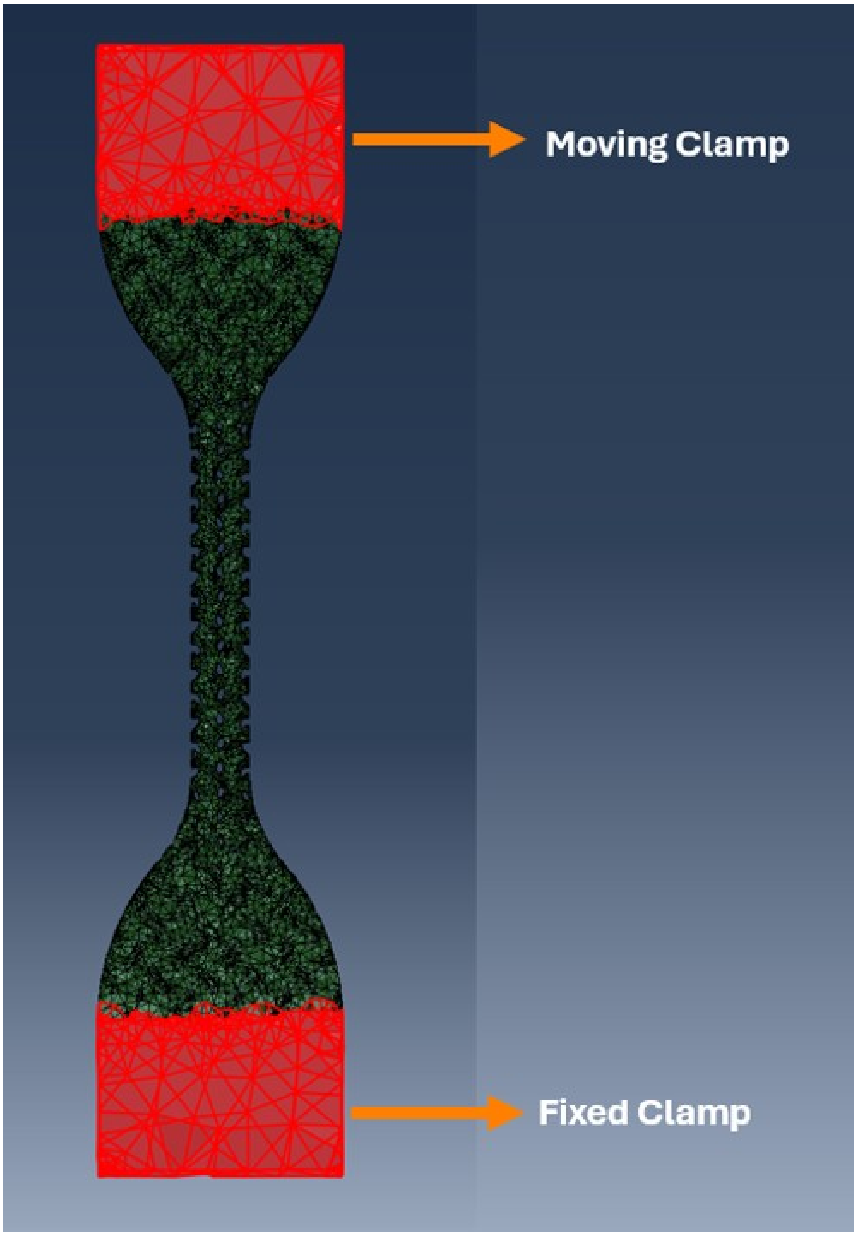

Figure 3.7: Finite element model of the tensile specimen showing the mesh distribution and clamp boundary regions.

The material properties were assigned to the entire specimen using the experimentally obtained uniaxial tensile test data. The material behaviour was implemented using a hyperelastic formulation based on the available experimental data.

Hyperelastic material models are typically used for materials that undergo large elastic deformations and exhibit nonlinear stress–strain behaviour.

Figure 3.8 shows the definition of the hyperelastic material model in Abaqus. The experimental nominal stress–strain data obtained from the solid tensile specimens were used to calibrate the Yeoh strain energy potential, which was then assigned to the lattice specimen for the FE simulation.

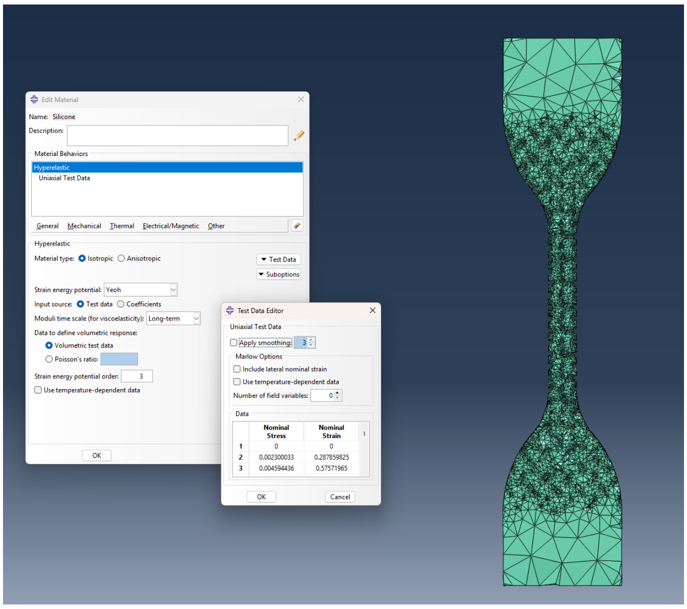

Figure 3.8: Definition of the hyperelastic material model in Abaqus using uniaxial tensile test data. The experimental nominal stress–strain data are used to calibrate the Yeoh strain energy potential for the lattice specimen.

The lower clamp was fully constrained using an encastre boundary condition to prevent rigid body motion of the specimen. A displacement was applied to the upper clamp in the loading direction to replicate the tensile elongation observed in the experimental test. The displacement was applied through the defined surface or reference node associated with the moving clamp. A displacement-controlled loading approach was adopted to ensure numerical stability and convergence during the simulation, particularly under large deformation conditions.

Figure 3.9 shows the boundary conditions applied to the tensile specimen in Abaqus. The lower region was fully constrained using an encastre condition, while displacement was applied at the upper clamp to simulate uniaxial tensile loading.

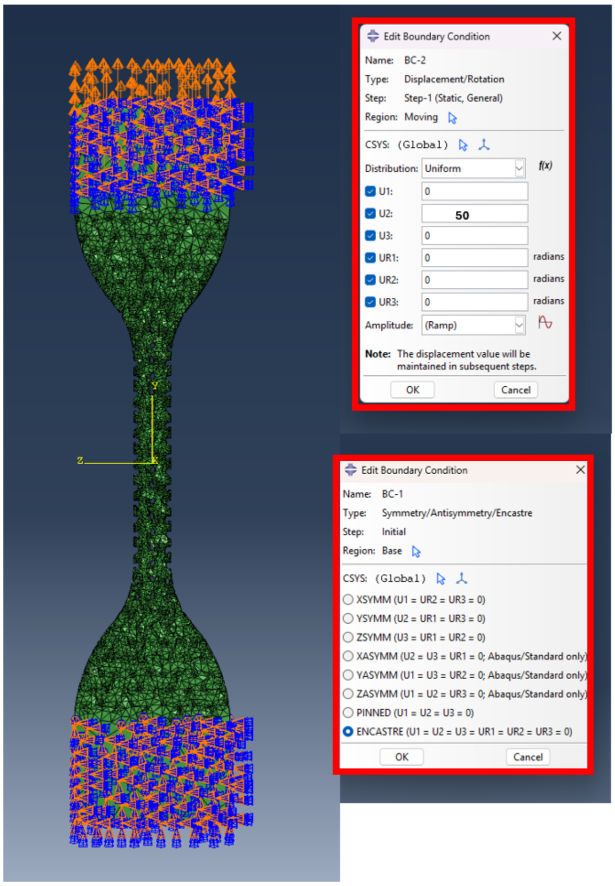

Figure 3.9: Boundary conditions applied to the tensile specimen. The lower region is fully constrained using an encastre condition, while a displacement is applied at the upper clamp to simulate uniaxial tensile loading.

3.5 FE Simulation Outputs

The FE simulation was used to obtain a preliminary prediction of the mechanical response of the gyroid specimen under tensile loading. The main outputs considered at this stage included the overall deformation pattern, stress distribution within the lattice region, and the force–displacement response of the structure. These outputs were used to identify how the gyroid architecture deforms under loading and whether stress concentrations appear near the gauge region or transition zones. A detailed comparison between the simulation and experimental results is presented later in the results and validation chapter.

4 Experimental Limitations and Observations

During the tensile testing and fabrication of the elastomeric specimens, several practical limitations were encountered that influenced both the experimental procedure and the interpretation of the measured data. The main limitations were related to premature failure near the lattice–solid transition region, specimen slippage, preloading effects, machine extension range, dimensional inaccuracies after printing, post-processing damage in thin gyroid structures, and the need to modify the gripping region of the tensile specimens.

These observations were important because they affected how the experimental results were interpreted and how later specimen designs were improved. Although the limitations did not prevent mechanical characterization, they introduced practical constraints that had to be considered when comparing the experimental response with the numerical simulation results.

4.1 Premature Failure at the Lattice–Grip Transition

During the initial stage of specimen development, the transition between the gyroid lattice gauge region and the solid gripping sections was designed with a relatively sharp geometric change. Although this configuration was the ASTM standard, it introduced a sudden change in stiffness between the lattice structure and the surrounding solid body.

When tensile tests were performed using this initial design, failure consistently occurred near the interface between the lattice region and the solid gripping section. Instead of deforming uniformly within the gauge region, the specimen fractured at the transition edge. This was problematic because the measured response would mainly represent the failure of the transition region rather than the mechanical behaviour of the gyroid lattice within the gauge section. As a result, the test would not provide a reliable characterization of the intended gyroid structure.

This behaviour indicated the presence of localized stress concentrations caused by the abrupt change in geometry and mechanical stiffness between the two regions.

Figure 4.1 shows the premature failure observed in the initial specimen design. The fracture occurred close to the transition between the lattice gauge region and the solid gripping section, confirming that the sharp transition created a weak region during tensile loading.

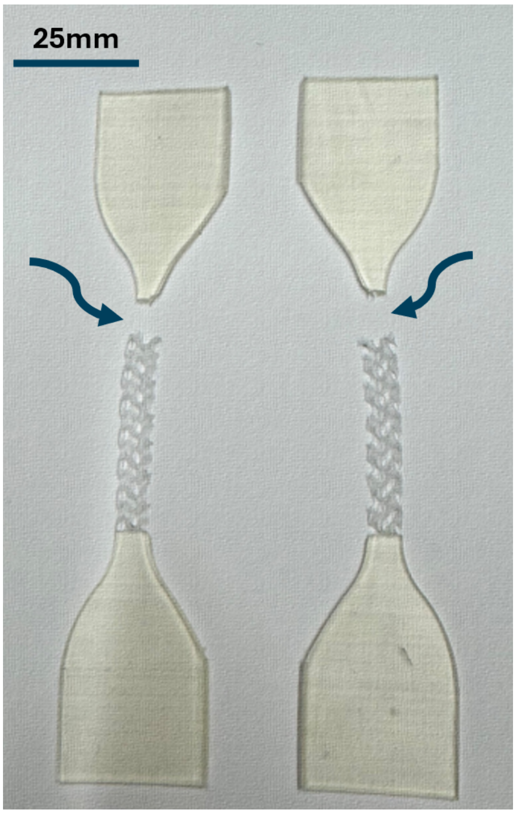

Figure 4.1: Initial tensile specimens showing premature failure.

To address this issue, the specimen geometry was modified to introduce a smoother transition between the lattice structure and the solid gripping sections. Instead of connecting the gyroid lattice directly to the solid body, a gradual transition was implemented using a ramp function within the nTop implicit modelling environment.

The ramp function enabled a progressive variation of the lattice parameters along the specimen length, creating a graded transition between the solid and lattice regions. By reducing the abrupt change in stiffness, the stress distribution along the specimen became more uniform during tensile loading. Similar ramp-based transition approaches for lattice tensile specimens have also been reported in previous TPMS lattice characterization studies [55].

Figure 4.2 illustrates the updated specimen design used for the tensile testing of the gyroid structure. The central region is the gyroid gauge section, where the main deformation is intended to occur during loading. The upper and lower transition regions gradually connect this gyroid region to the solid gripping sections, reducing the abrupt stiffness change that was observed in the initial design.

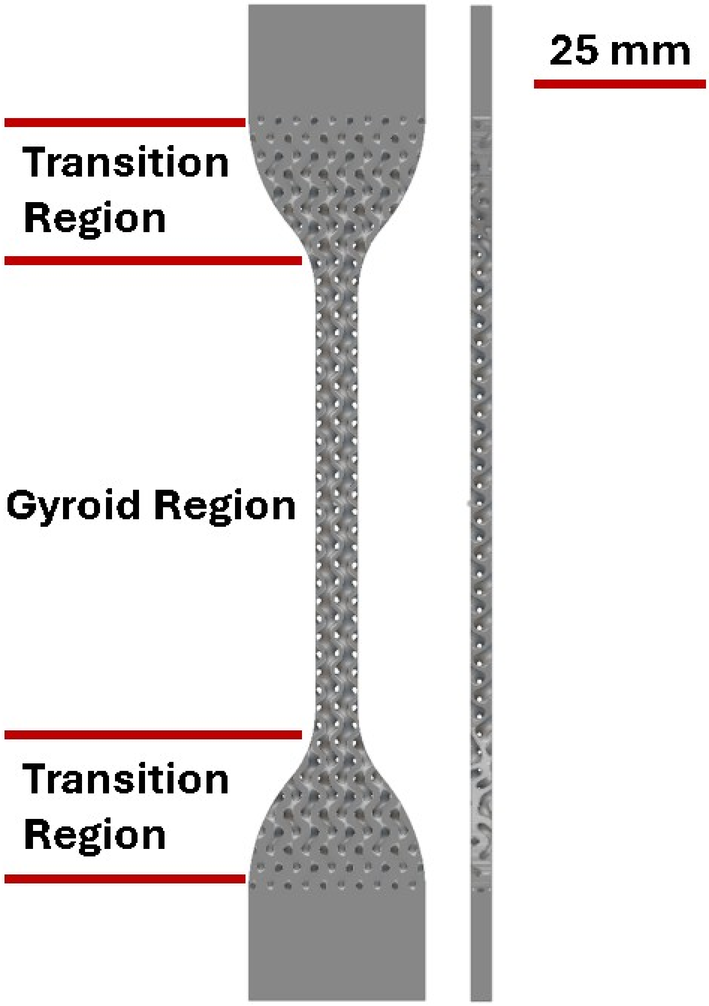

Figure 4.2: Updated gyroid specimen design showing the central gyroid gauge region and the transition regions between the lattice structure and the solid gripping sections.

The transition was generated in nTop using field-based operations. A ramp function was used to vary the gyroid thickness gradually along the specimen length, while clamp operations were used to limit the minimum and maximum values of the thickness field. This allowed the lattice to change progressively from the solid section into the gyroid gauge region, producing a smoother transition and reducing stress concentration near the grip–lattice interface.

4.2 Tensile Testing Challenges and Specimen Modification

During tensile testing, one of the main experimental challenges was specimen slippage within the clamps of the testing device. The grips available on the texture analyser were not specifically designed for soft elastomer materials such as silicone and flexible photopolymer resins. In standard tensile testing of rubber-like materials, specialized grips with serrated or pneumatic clamping mechanisms are commonly used to prevent slippage and ensure stable load transfer.

Due to the absence of such specialized grips in the present setup, the specimens occasionally experienced minor sliding within the clamps during the initial loading stage. This affected the stability of the tensile test and introduced uncertainty in the initial portion of the recorded force–displacement data. Figure 4.3 shows an example of specimen movement near the gripping region during tensile testing. Figure 4.3(i) shows the specimen before noticeable sliding, while Figure 4.3(ii) shows the specimen after movement within the clamp region. This confirmed that part of the initial crosshead displacement was affected by grip movement rather than only material deformation.

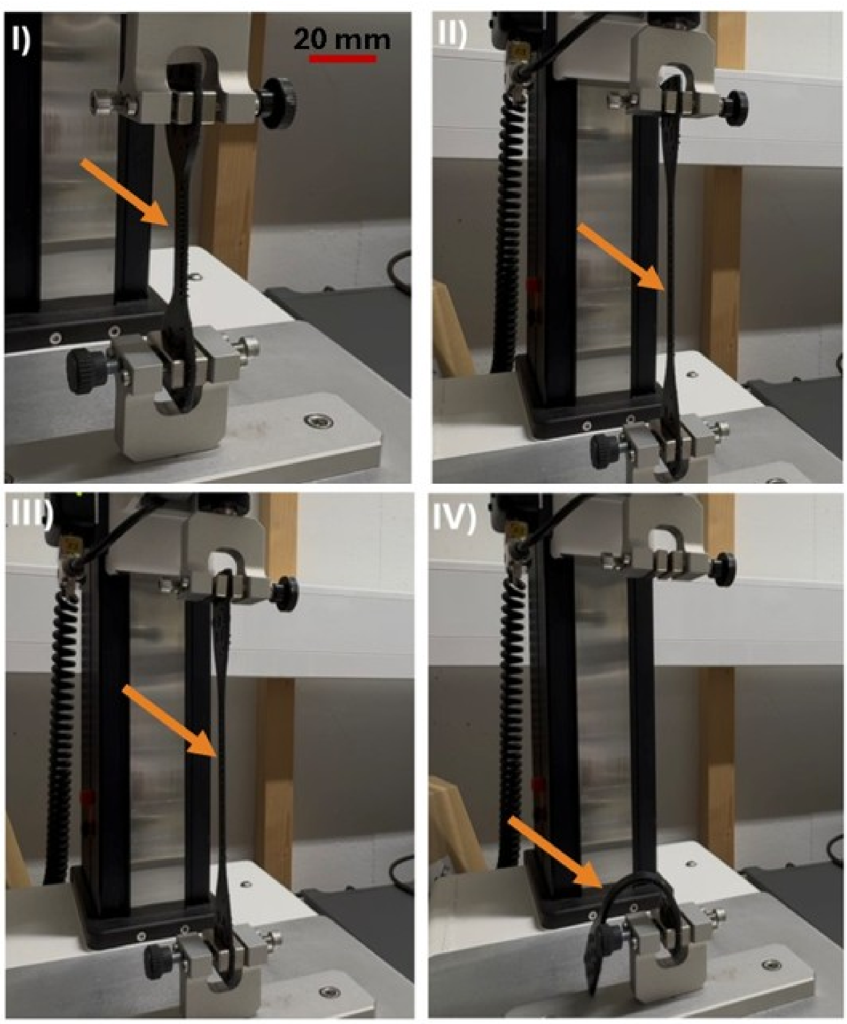

Figure 4.3: Example of specimen slippage during tensile testing: (i) specimen position before noticeable sliding and (ii) specimen position after movement within the clamp region.

A related effect observed in the force–displacement curves was the presence of a short preloading region. In several tests, measurable elongation of the specimen began only after a small displacement had already occurred. This behaviour was mainly caused by minor adjustment of the specimen inside the clamps before stable load transfer was established. Figure 4.4 shows this initial preloading stage. Figure 4.4(i) shows the specimen at the beginning of loading, where slack and clamp adjustment were still present. Figure 4.4(ii) shows the specimen after the preload adjustment, where the sample was more fully engaged in the loading direction.

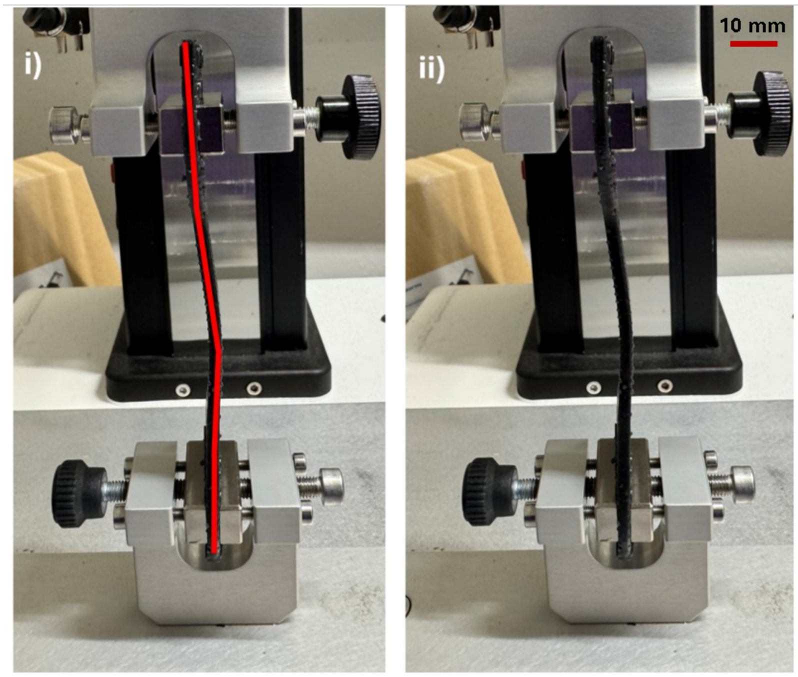

Figure 4.4: Representative example of the preloading region observed at the beginning of tensile testing: (i) initial specimen position before full engagement and (ii) specimen position after preload adjustment.

To reduce specimen slippage, the dog-bone tabs were first modified by adding transverse ribs to the gripping region. The purpose of these ribs was to create a mechanical interlock between the soft specimen and the clamp surfaces, rather than relying only on friction. Figure 4.5 shows the first modified dog-bone design with integrated transverse ribs. Figure 4.5(i) shows the overall dog-bone geometry, while Figure 4.5(ii) highlights the ribbed gripping region intended to improve clamp engagement.

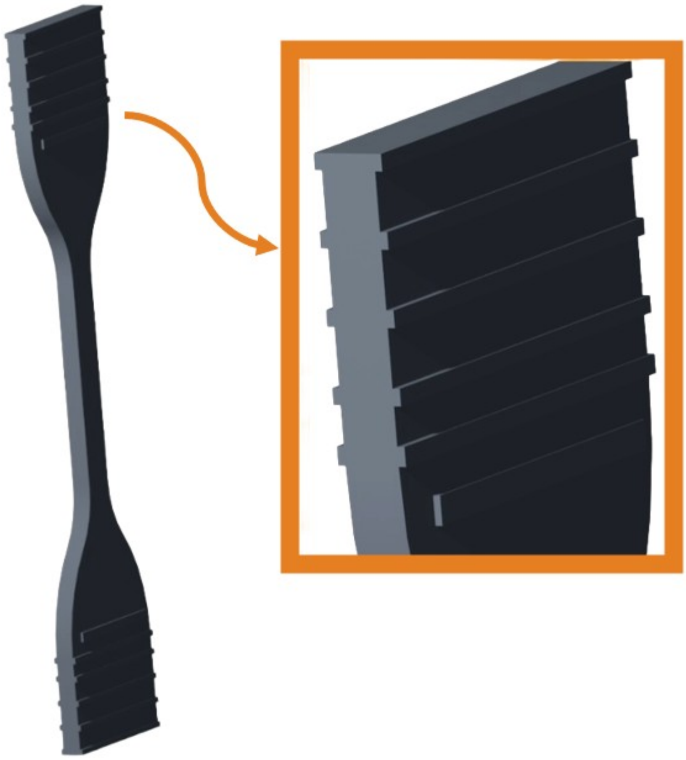

Figure 4.5: CAD model of the modified dog-bone specimen with integrated transverse ribs: (i) overall specimen geometry and (ii) ribbed gripping region designed to enhance mechanical interlocking.

However, this modification did not fully solve the gripping issue and introduced a new failure region. The ribs acted as local stress concentrators, and because the soft resins had relatively low tear resistance, the added features were damaged or sheared under the clamping pressure before the specimen reached its actual breaking point. Figure 4.6 shows the localized rib damage observed after testing. Figure 4.6(i) shows the damaged gripping region after the test, while Figure 4.6(ii) shows the local shearing and flattening of the rib features.

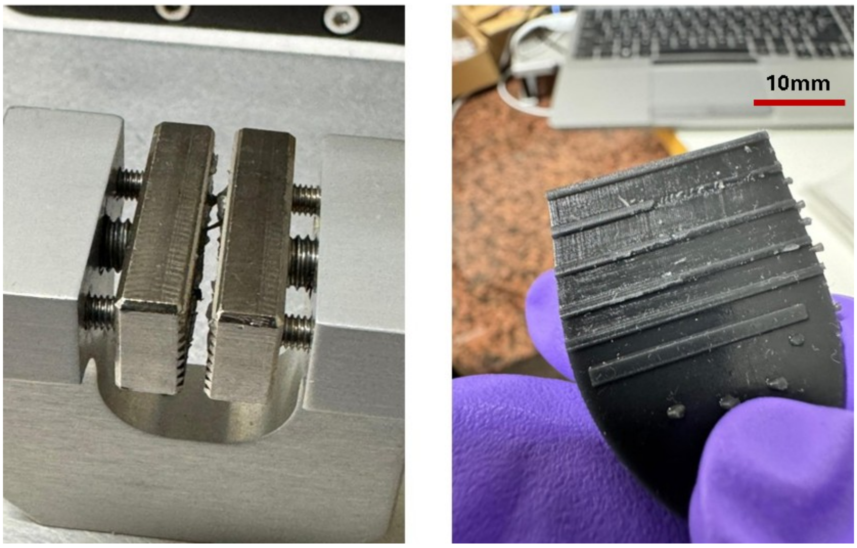

Figure 4.6: Failed gripping modification after tensile testing: (i) damaged gripping region and (ii) localized rib shearing and flattening caused by clamping pressure.

Based on these observations, a second modified specimen geometry was introduced to improve clamp stability without creating severe local stress concentration. Figure 4.7 shows the final modified gripping geometry used in the later tensile tests. This design improved specimen engagement in the clamps and reduced the likelihood of premature failure caused by local damage at the gripping region.

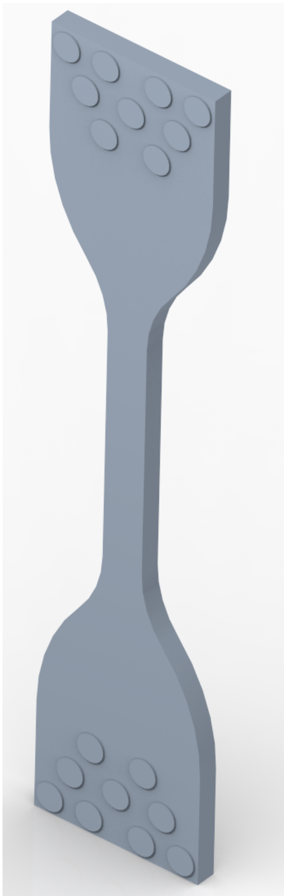

Figure 4.7: Final modified specimen geometry incorporating additional gripping features to improve clamp stability during tensile testing.

4.3 Specimen Length and Machine Extension Limitations

An additional limitation was related to the overall length of the Flexible 80A specimens and the available extension range of the TA.XTplus Texture Analyser. During the initial uniaxial tensile testing, the testing machine reached its maximum extension range at approximately 150% strain for the Flexible 80A resin specimens. However, the specimen did not fracture within this available displacement range.

As a result, the complete failure behaviour of the material could not be captured during the initial test configuration. The recorded stress–strain curves therefore represented the material response only within the accessible deformation range rather than the full elongation-to-break behaviour. To address this limitation, the specimen type and geometry were later adjusted to obtain more useful tensile data within the displacement capability of the testing device.

4.4 Dimensional Inaccuracies in Printed Specimens

One limitation observed during specimen preparation was the dimensional variation between the designed and printed samples. Although the specimens were designed according to the required tensile testing geometry, small dimensional deviations were observed after fabrication and post-processing. In particular, the vertical length of the printed specimen increased by approximately 0.1 to 1 mm compared to the intended design dimension.

This dimensional change can be attributed to factors such as resin curing behaviour, support removal, printer resolution, and post-curing deformation. Although the deviation was relatively small, it is still important to consider because dimensional accuracy affects the gauge length, strain calculation, and comparison between experimental and simulation results. Therefore, the measured specimen dimensions were considered during the interpretation of the tensile response.

4.5 Post-Processing Damage in Thin Gyroid Structures

The wall thickness of the gyroid lattice was an important parameter during fabrication. Initial tests were performed using wall thicknesses ranging from 0.5 mm to 1 mm. While these structures were successfully printed, challenges were observed during the removal of support structures, particularly for the softer Silicone 40A specimens.

During post-processing, the removal of support structures can introduce local surface defects in thin lattice geometries. In the present gyroid samples, several support regions remained partially attached after removal, while other regions experienced small material damage caused by cutting and detachment. These imperfections were particularly critical for thin TPMS structures, where local damage may affect structural integrity and functional performance.

Figure 4.8 shows the surface imperfections observed after support removal. These defects indicate that thin gyroid walls are sensitive to post-processing, especially when the support regions are large relative to the local wall thickness of the structure.

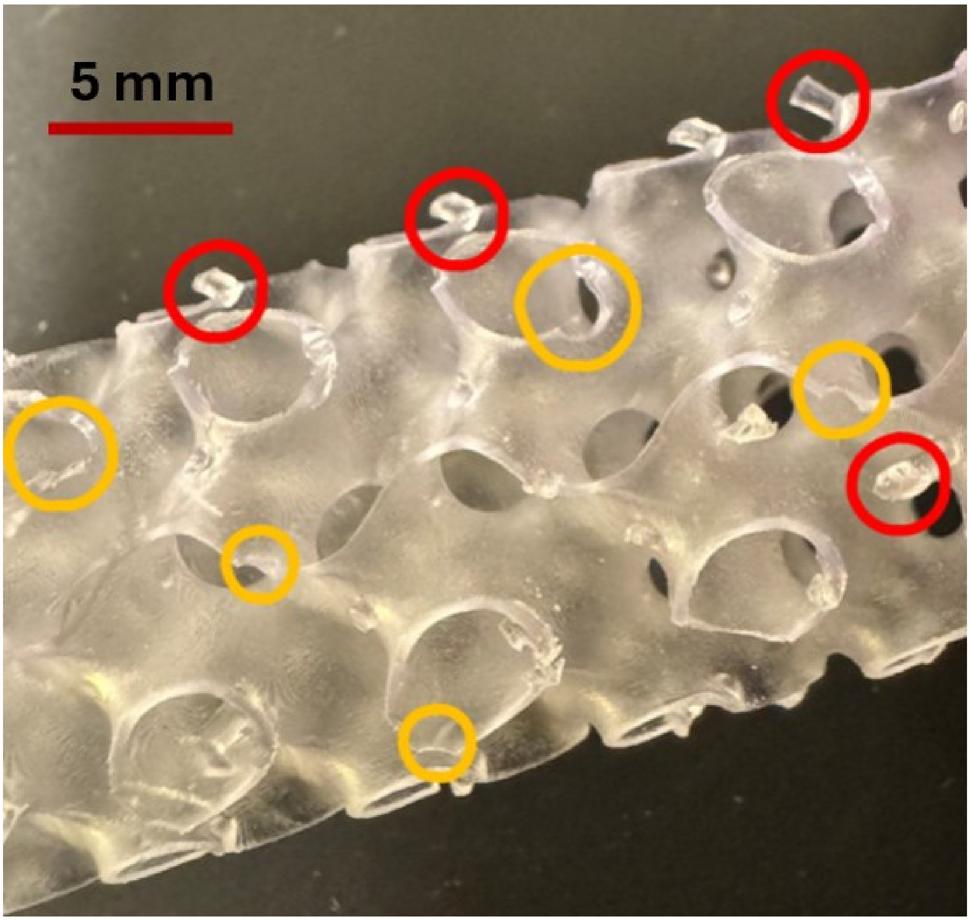

Figure 4.8: Support contact regions and surface imperfections observed after support removal in a printed gyroid structure. This is flexible 80A elastomer.

The Silicone 40A structures were especially sensitive during post-processing because of their low stiffness and high compliance. If the support structures were larger or stronger than the local gyroid wall section, the gyroid could tear or break during support removal. Therefore, the post-processing stage had to be performed carefully, and the minimum wall thickness of the gyroid structure became an important fabrication limitation. To reduce this issue, the support size was optimized, while the wall thickness of the gyroid structures was maintained between 0.8 mm and 1 mm. This balance ensured sufficient structural strength during fabrication while minimizing the risk of damage during support removal.

5 Results and Validation

This chapter presents the results obtained from the experimental material testing, hyperelastic material model fitting, FE simulation, and experimental validation of the gyroid samples. The main purpose of this chapter is to validate whether the selected material model and FE simulation workflow can reasonably represent the mechanical behaviour of the printed Silicone 40A gyroid structures under tensile loading.

The results are presented in two main stages. First, solid dog-bone tensile specimens were tested to obtain the base material properties required for hyperelastic material model fitting. These material properties were then used in the FE simulations of the gyroid structure. Second, the printed gyroid specimens were tested experimentally and compared with the simulation results to evaluate the accuracy of the numerical model.

5.1 Dog-Bone Tensile Test Results

The tensile behaviour of the printed elastomeric materials was first evaluated using solid dog-bone tensile specimens. These tests were performed on the solid sample rather than the gyroid specimens. The purpose of the dog-bone tests was to obtain the stress–strain response of the solid printed materials so that suitable material properties could be taken and used as input data for the FE simulations.

The dog-bone tensile test results were therefore used mainly for material characterization and hyperelastic model fitting. This step was necessary because the simulations require a material model that could describe the nonlinear elastic behaviour of the printed elastomeric material under tensile loading.

As shown in Figure 5.1 the average experimental stress–strain data obtained from three repeated tests for each test sample. This averaging was used to provide a more representative response for comparison and model fitting.

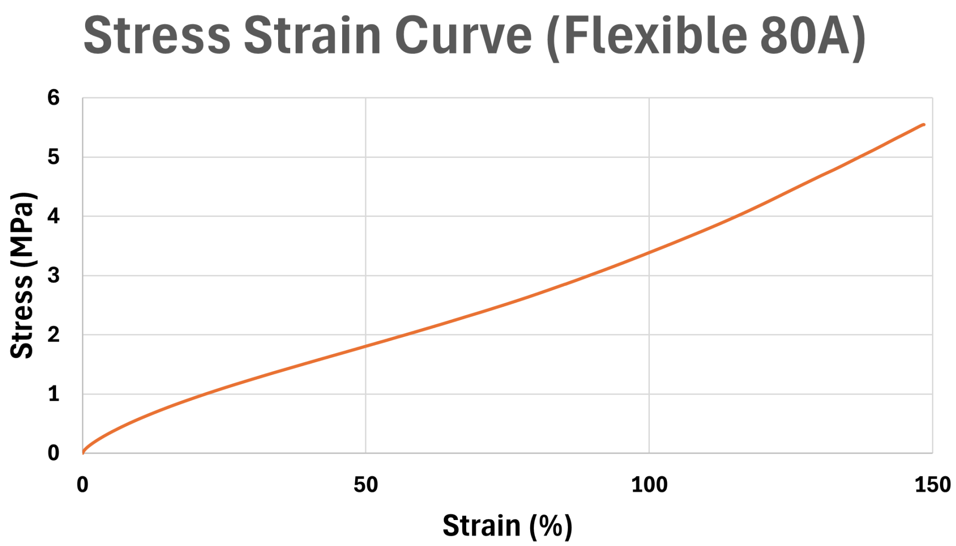

Figure 5.1: Experimental stress–strain curves obtained from tensile testing of solid Flexible 80A dog-bone specimens.

The material exhibits nonlinear elastic behaviour, which is typical of elastomeric polymers. The measured curves from the three tested specimens show good agreement with each other, indicating consistent mechanical performance of the printed samples.

Figure 5.2 presents the stress–strain behaviour of the solid Silicone 40A dog-bone specimens.

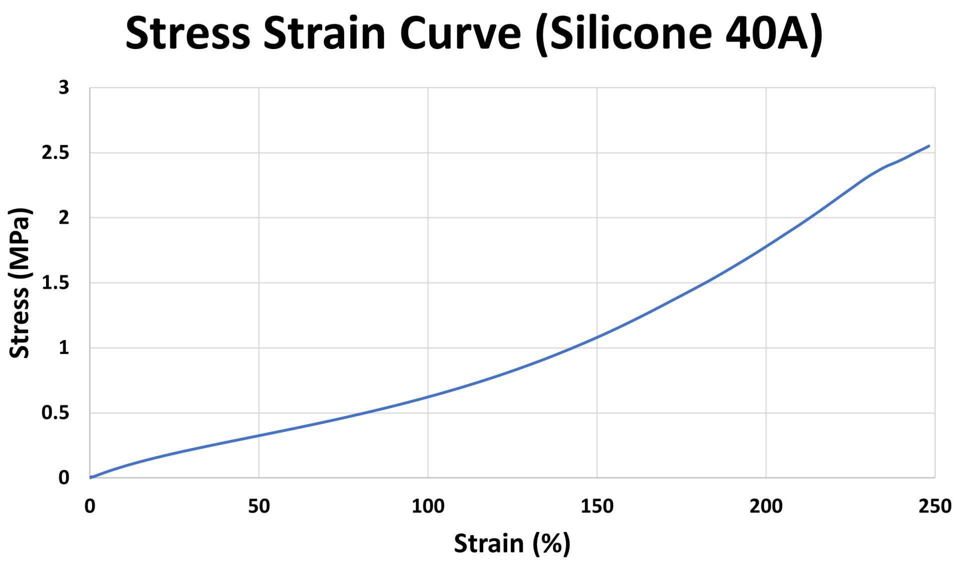

Figure 5.2: Experimental stress–strain curves obtained from tensile testing of solid Silicone 40A dog-bone specimens.

Compared with Flexible 80A, the Silicone 40A specimens demonstrate a significantly larger strain capability while maintaining a lower stress response. The experimental results from the three tested specimens show a peak stress of approximately 2.5 MPa, with elongation values exceeding 250%. These results confirm the highly flexible nature of the Silicone 40A material and its suitability for applications requiring large elastic deformation.

The dog-bone tensile test results confirmed that both materials exhibit nonlinear elastomeric behaviour. However, Silicone 40A showed higher elongation capability, making it more suitable for highly deformable gyroid structures and soft sensing applications.

As shown in Figure **??**, error bars indicating the standard deviation between the tested specimens.

5.1.1 Material Model Fitting Results

After obtaining the experimental uniaxial tensile data from the solid Silicone 40A dog-bone specimens, the data were imported into Abaqus for hyperelastic material model fitting. Abaqus performs a curve-fitting procedure to determine the material parameters that best match the measured stress–strain behaviour. The fitting process minimizes the difference between the experimental data and the predicted response of the selected hyperelastic model.

The tensile test data was evaluated for the model fitting of different hyper-elastic models but the stress-strain curve satisfies the polynomial model of degree 3 (Yeoh Model) as shown in the figure 5.3.

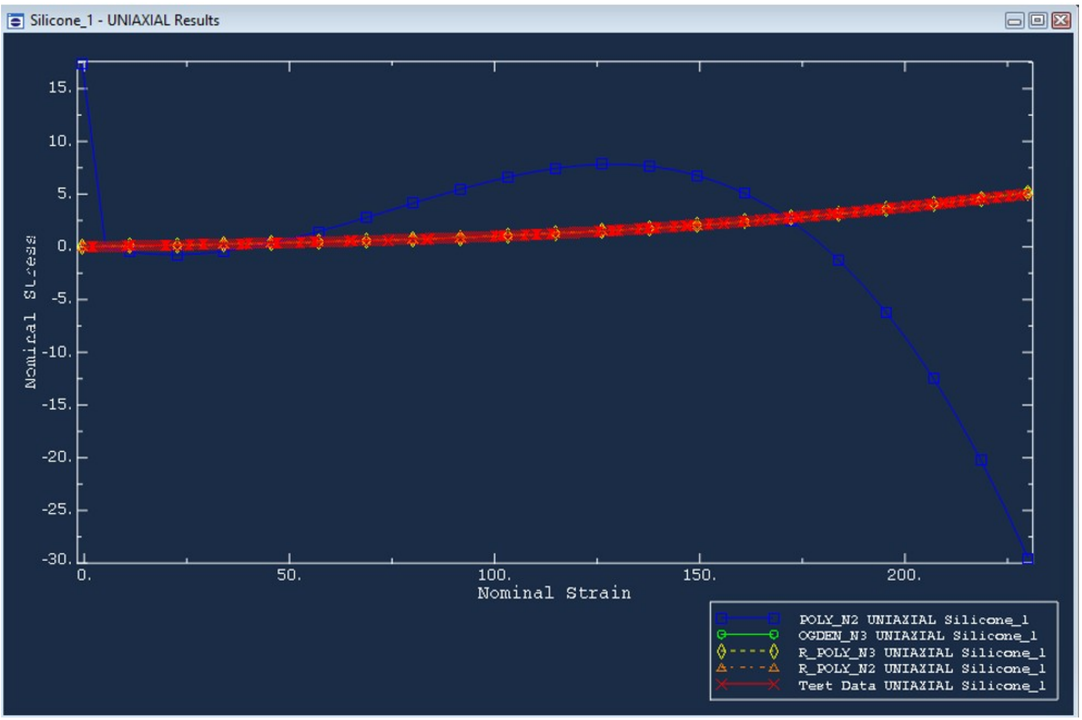

Figure 5.3: Evaluation of hyperelastic material models in Abaqus showing the comparison between experimental dog-bone tensile test data and fitted constitutive models, together with the stability limits of the selected model.

Table 5.1 summarizes the material coefficients and stability output obtained from the Abaqus material evaluation window. The selected model was the third-degree reduced polynomial formulation, also referred to as the Yeoh model. The fitted model was reported as stable for the evaluated uniaxial, biaxial, planar, and volumetric deformation modes.

Table 5.1: Material parameters and stability information for the selected Yeoh model.

Parameter	**Value / Description**
Material	Silicone 40A
Test data	Uniaxial tensile test data from solid dog-bone specimens
Selected model	Reduced polynomial model, $N = 3$ (Yeoh model)
C_{10}	3.3375×10^{-3}
C_{20}	8.4017×10^{-8}
C_{30}	-1.5832×10^{-13}
D_1, D_2, D_3	0
Model stability	Stable for all evaluated strain modes
Volumetric stability	Stable for all evaluated volume ratios

The third-degree Yeoh model was selected for the gyroid simulation because it provided a stable fit for the available uniaxial tensile data and was suitable for representing the nonlinear response of the Silicone 40A material. Since the fitting was based only on uniaxial dog-bone tensile data, the model was expected to provide a reasonable approximation of the tensile response. However, some deviation was expected when applying the model to the gyroid structure because the gyroid specimen experiences a more complex deformation state involving stretching, bending, and local deformation of the lattice walls.

5.2 Gyroid FE Simulation Results

The FE simulation was carried out to predict the mechanical response of the Silicone 40A gyroid specimen under tensile loading. The material properties used in the simulation were obtained from the solid dog-bone tensile tests and the fitted Yeoh hyperelastic model described in the previous section.

The main outputs considered in the simulation included the overall deformation pattern, stress distribution within the gyroid lattice region, and the stress–strain response of the structure. These outputs were used to understand how the gyroid architecture deforms under tensile loading and to provide a numerical result for comparison with the experimental test of the printed gyroid specimen.

Figure 5.4 shows the predicted deformation of the gyroid specimen under tensile loading. The deformation is mainly concentrated within the gyroid lattice gauge region, while the solid gripping sections remain comparatively stable. This indicates that the specimen design successfully directs deformation toward the intended lattice region, allowing the mechanical response of the gyroid architecture to be evaluated.

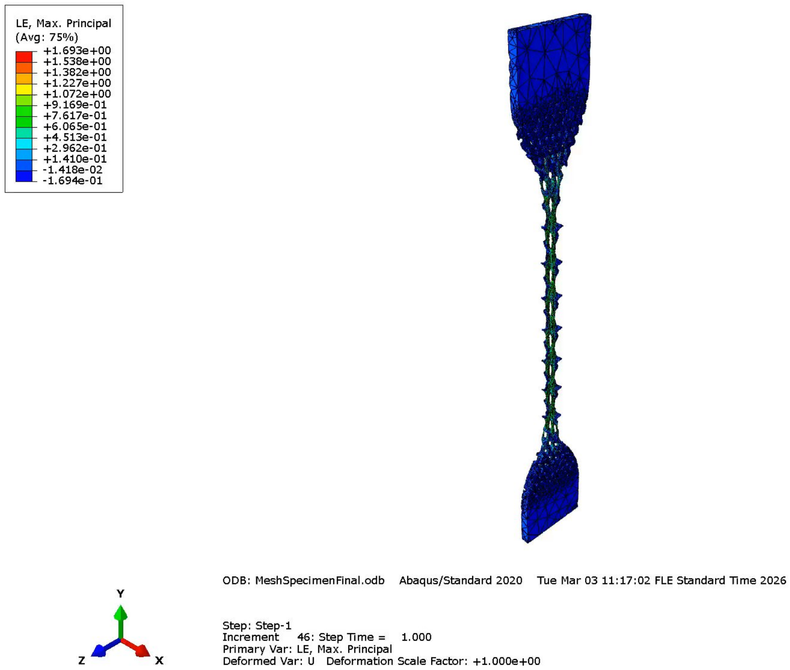

Figure 5.4: FE simulation showing the predicted deformation and stress distribution of the Silicone 40A gyroid structure under tensile loading.

The simulation also provides an estimate of the stress distribution within the lattice structure. This is useful for identifying regions where stress concentration may occur during tensile loading. In the present model, the simulation results were mainly used to evaluate the overall deformation behaviour of the gyroid specimen and to support comparison with the experimental tensile response of the printed gyroid sample.

5.3 Experimental Results and Simulation Comparison of Gyroid Samples

The fabricated Silicone 40A gyroid samples were experimentally tested under tensile loading to evaluate their mechanical response and compare the physical behaviour with the FE simulation results. Unlike the dog-bone tests, which were performed on solid specimens to obtain material properties, this test was performed directly on the printed gyroid specimen to assess the behaviour of the lattice structure.

During testing, the gyroid structure showed large deformation capability due to the combination of the soft Silicone 40A material and the compliant TPMS architecture. The experimental response confirmed that the lattice gauge region was able to deform under tensile loading while maintaining structural continuity. Practical effects such as specimen slippage, preloading, dimensional variation, and post-processing imperfections may have influenced the measured response and were considered when interpreting the results.

The experimental stress–strain curve obtained from the gyroid tensile test was compared with the FE simulation result generated using the calibrated Yeoh hyper-elastic material model. This comparison was important because the simulation used material properties obtained from solid dog-bone tensile specimens, while the gyroid specimen experienced a more complex deformation response due to its internal lattice architecture.

Figure 5.5 compares the experimental and simulated stress–strain response of the Silicone 40A gyroid structure. The experimental curve represents the averaged response obtained from gyroid specimen tests, while the simulation curve represents the FE prediction results.

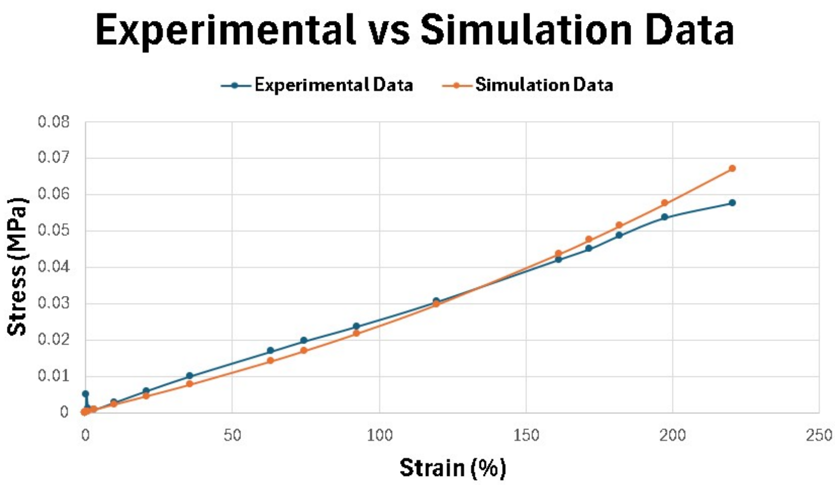

Figure 5.5: Comparison of experimental and simulation stress–strain curves for the Silicone 40A gyroid structure.

The experimental and simulation results show a similar trend in the initial and intermediate strain regions. Up to approximately 100% strain, both curves follow a comparable response. For example, at 92.477% strain, the experimental stress is approximately 0.0236 MPa, while the simulation predicts approximately 0.0217 MPa. This gives an absolute error of 0.0019 MPa, indicating good agreement in the early deformation region.

As the strain increases further, a more noticeable difference appears between the two curves. At the maximum evaluated strain of approximately 220.51%, the experimental stress reaches approximately 0.0576 MPa, whereas the simulation predicts approximately 0.0670 MPa. This gives an absolute error of 0.0094 MPa. The relative error at this maximum strain point can be calculated using Equation 5.1.

$$\text{Relative error} = \frac{|\sigma_{\text{simulation}} - \sigma_{\text{experimental}}|}{\sigma_{\text{experimental}}} \times 100 \tag{5.1}$$

Using the stress values at the maximum strain point:

$$\text{Relative error} = \frac{|0.0670 - 0.0576|}{0.0576} \times 100 = 16.3\% \tag{5.2}$$

Therefore, the simulation overpredicts the experimental stress by approximately 16.3% at the maximum evaluated strain. Over the full comparison range, the mean absolute error between the experimental and simulation data is approximately 0.0025 MPa, while the root mean square error is approximately 0.0033 MPa.

Overall, the comparison shows that the FE model provides a reasonable approximation of the gyroid specimen behaviour, particularly in the initial and intermediate strain regions. Although some deviation occurs at higher strain, the model is still useful for predicting the general deformation trend and mechanical response of the printed Silicone 40A gyroid structure.

The difference observed between the simulation and experimental results at higher strain levels can mainly be linked to the modelling and testing limitations considered in this study. The third-degree Yeoh model was defined using only uniaxial dog-bone tensile test data. Although this provides a suitable approximation of the base Silicone 40A material response, it may not fully represent the multi-axial deformation behaviour of the gyroid structure under large strains.

Additionally, the use of a coarse mesh in the simulation can result in a slightly stiffer response due to reduced geometric accuracy. Since the gyroid structure contains thin walls and curved surfaces, mesh resolution plays an important role in accurately capturing local deformation. A coarser mesh may simplify the curved geometry and reduce local flexibility, which can contribute to overprediction of stress at higher strain levels.

6 Pressure Sensor Demonstration

This chapter presents the experimental evaluation of the pneumatic pressure sensing system. The chapter is divided into three main parts. First, the working principle and measurement setup of the multi-sensor pneumatic system are introduced. Second, the response of the gyroid-based sensor is evaluated under localized touchpoint loading. Third, comparative demonstrations are presented to evaluate the effect of different internal structures, including empty, sponge-based, and gyroid-based configurations, followed by a comparison between gyroid structures with different cell sizes.

6.1 Sensor Concept and Working Principle

The pneumatic sensor concept is based on measuring pressure variations generated by local deformation of a soft internal structure. In this system, the sensing region is connected to a constant pneumatic supply at the inlet and exposed to atmospheric pressure at the outlet. When an external load is applied to the sensing region, the internal structure deforms and changes the local airflow and pressure distribution inside the pneumatic pathway.

The pressure changes are measured using multiple pressure gauges positioned at different locations along the pneumatic pathway. This distributed sensing arrangement allows the system to capture not only the magnitude of the pressure response, but also how the response varies spatially between different measurement positions.

Therefore, the sensor output can provide information about localized touchpoint interactions rather than only a single global pressure change.

In this study, the gyroid structure was investigated as an internal sensing architecture because its continuous TPMS geometry can deform under applied loading while maintaining interconnected pathways for airflow. For comparison, empty-channel and sponge-based configurations were also evaluated to understand how different internal structures influence the pressure response.

6.2 Circuit Design and Measurement Method

The electrical circuit consists of multiple pressure gauges interfaced with an Arduino Mega 2560 using a distributed I^2C communication approach. The wiring is organized such that each pressure gauge receives a stable power supply while maintaining independent communication lines for accurate data acquisition.

Figure 6.1 shows the circuit schematic used for connecting the pressure gauges to the Arduino Mega 2560. The figure illustrates how power, ground, and communication lines were arranged for distributed pressure measurement.

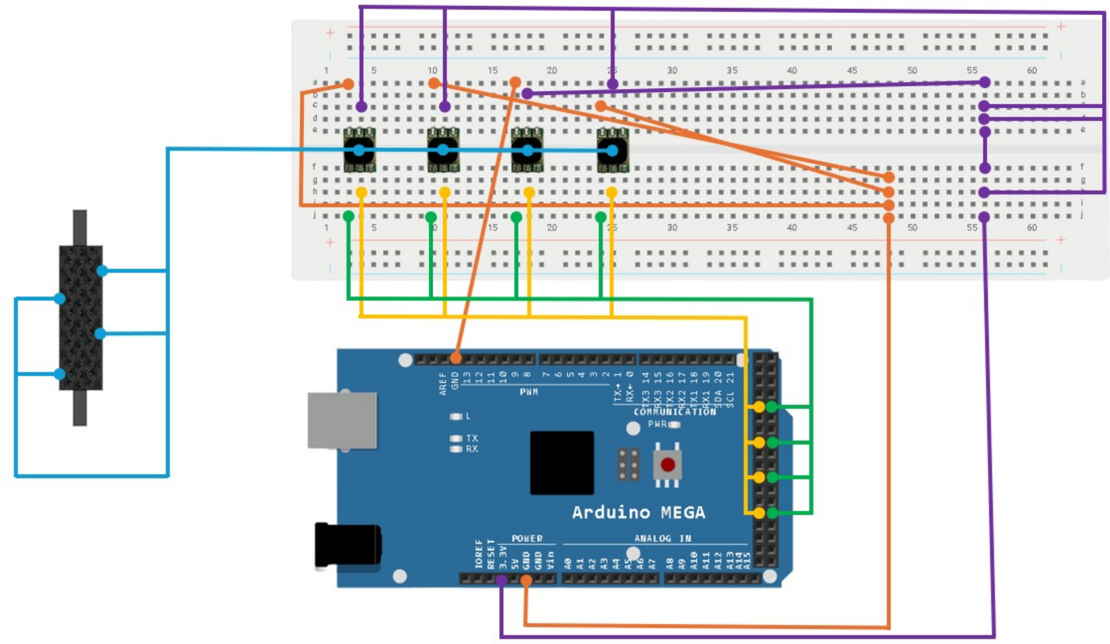

Figure 6.1: Circuit schematic showing the connection of multiple pressure gauges with the Arduino Mega 2560 for distributed pressure measurement.

Pin 1 of each pressure gauge is connected to ground. The supply voltage of 3.3 V is provided from the Arduino and distributed to all pressure gauges through pin 2.

Each pressure gauge communicates with the microcontroller using dedicated I^2C lines. Pin 5 (SDA) and pin 6 (SCL) of each pressure gauge are connected to separate digital pins on the Arduino. This configuration allows multiple pressure gauges with identical I^2C addresses to be operated simultaneously by assigning them to independent buses.

The Arduino acts as the master device, initiating communication with each pressure gauge sequentially. The pressure gauges measure the pressure variation within the pneumatic system and transmit the corresponding digital data to the microcontroller. These values are then processed and recorded over time for further analysis.

The pressure gauge used in this system follows a standard 6-pin configuration

[56]. The relevant pins utilized in this setup are described in Table 6.1.

Table 6.1: Pressure gauge pin connections used in the measurement circuit.

Pin Number	**Function**	**Connection**
Pin 1	Ground (GND)	Arduino GND
Pin 2	Supply voltage (V_{DD})	3.3 V supply
Pin 5	SDA data line	Arduino digital pins
Pin 6	SCL clock line	Arduino digital pins

6.3 Gyroid Sensor Demonstration Setup

The performance of the pneumatic pressure sensor was evaluated using four pressure gauges. The gyroid structure was encapsulated within a heat shrink (ChangYuan Group Ltd., China) and placed between a constant pneumatic supply at the inlet and an atmospheric outlet. Four touchpoints were taken on the sensing region, as shown in Figure 6.3, and localized pressing at these points produced pressure variations that were measured by the pressure gauges.

The four pressure gauges were connected to the pneumatic channels at different locations, which allowed distributed measurement of the pressure response. Figure 6.2 shows the implemented sensing system with the gyroid-based sensing region, pneumatic connections, and the four pressure gauges. The top of the structure is connected to the constant pneumatic supply, while the bottom remains exposed to atmospheric pressure. The pressure gauges are labelled as Pressure Gauge 1, Pressure Gauge 2, Pressure Gauge 3, and Pressure Gauge 4 according to their positions in the setup.

Figure 6.2 shows the implemented four-gauge pneumatic sensing setup. The figure identifies the gyroid sensing region, pneumatic connections, and the four pressure gauges used for distributed pressure measurement.

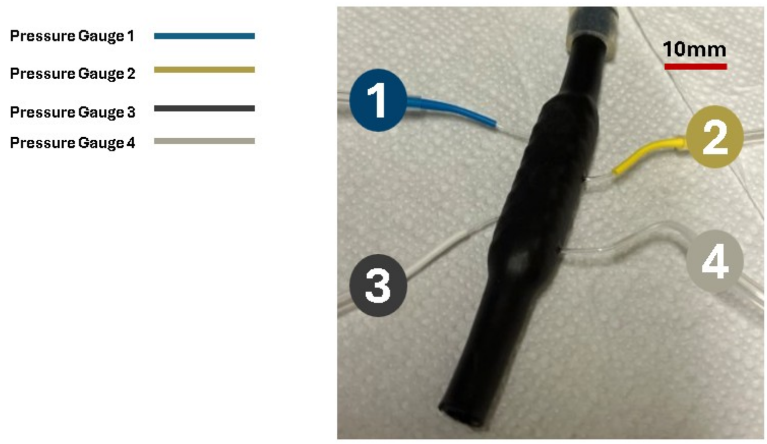

Figure 6.2: Four-gauge pneumatic setup used for distributed pressure measurement.

Figure 6.3 shows the touchpoint locations used during the gyroid sensor demonstration. These labelled points were used to apply localized loading at different positions on the sensing region.

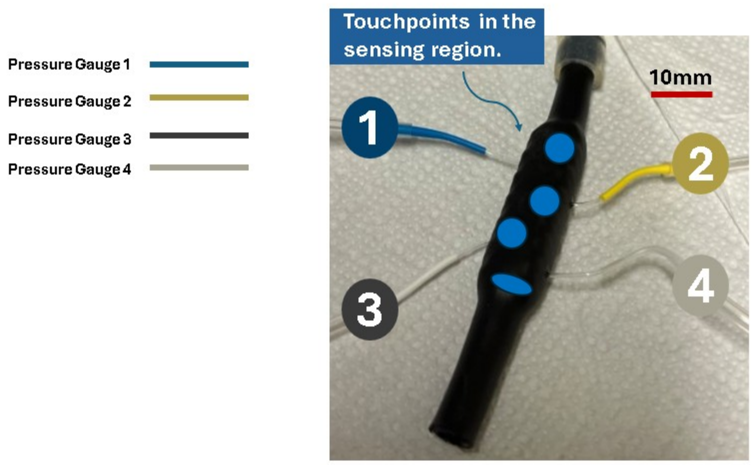

Figure 6.3: Touchpoint locations used during the pressure sensor demonstration.

6.4 Gyroid Sensor Demonstration Procedure

At the beginning of the experiment, the system was in a no-flow condition, and all four pressure gauges recorded values close to zero. The pneumatic supply was then turned on, creating continuous airflow through the gyroid structure. This airflow was able to pass through the sample because of the interconnected geometry of the gyroid architecture. After the airflow reached a stable operating condition, localized pressure was applied at the predefined touchpoints using a pencil tip. The resulting pressure changes were recorded continuously from all four pressure gauges.

The first significant rise in the pressure signals corresponds to the activation of the pneumatic supply, not to a touch interaction. Therefore, the initial increase represents the transition from a no-flow baseline to a steady airflow condition. The later disturbances in the pressure signals correspond to the touchpoint loading events.

6.4.1 Gyroid Sensor Time-Domain Response

Figure 6.4 shows the overall time-domain response of the four pressure gauges. The figure includes the initial pneumatic activation region and the four labelled touchpoint loading events.

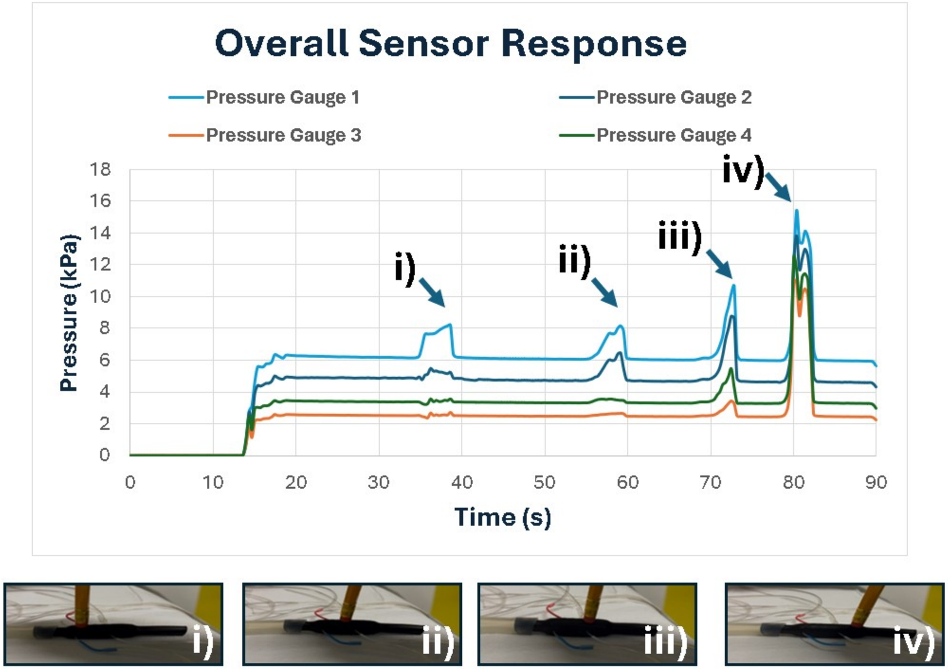

Figure 6.4: Overall time-domain response of the four pressure gauges during pneumatic activation and four labelled touchpoint loading events.

Before pneumatic activation, the four pressure gauges remained close to zero. In the recorded baseline region from 0 s to 13.340 s, the measured pressure values ranged from −0.0021 kPa to 0.0083 kPa for Pressure Gauge 1, 0.0007 kPa to 0.0090 kPa for Pressure Gauge 2, 0.0014 kPa to 0.0117 kPa for Pressure Gauge 3, and −0.0021 kPa to 0.0103 kPa for Pressure Gauge 4. This confirms that the system was initially stable before airflow was introduced.

The first notable increase begins at 13.683 s, when the pneumatic supply is activated. At this time, the recorded values were 0.0586 kPa, 0.0951 kPa, 0.0565 kPa, and 0.0924 kPa for Pressure Gauges 1–4, respectively. The pressure then increased rapidly, and at 14.367 s the values reached 2.7572 kPa, 2.7283 kPa, 1.7389 kPa, and 2.5076 kPa. This initial rise represents the transition from the no-flow baseline condition to the pressurized airflow condition inside the sensing structure.

The pressure peaks associated with the four labelled touchpoint interactions are summarized in Table 6.2. For each touchpoint, the table reports the maximum recorded pressure value for each pressure gauge within the corresponding loading event.

Table 6.2: Maximum recorded pressure values during the four labelled touchpoint interactions.

Touchpoint	**Pressure Gauge 1**	**Pressure Gauge 2**	**Pressure Gauge 3**	**Pressure Gauge 4**
i)	8.1937 kPa at 38.659 s	5.4834 kPa at 36.264 s	2.7179 kPa at 38.659 s	3.5777 kPa at 38.659 s
ii)	8.1413 kPa at 59.189 s	6.4363 kPa at 59.189 s	2.6483 kPa at 59.189 s	3.5729 kPa at 57.821 s
iii)	10.6407 kPa at 72.875 s	8.7688 kPa at 72.533 s	3.4322 kPa at 72.533 s	5.4689 kPa at 72.533 s
iv)	15.3932 kPa at 80.403 s	13.8143 kPa at 80.403 s	11.0426 kPa at 80.061 s	12.4609 kPa at 80.061 s

As shown in the table 6.2, touchpoint i), the highest response was recorded by Pressure Gauge 1, reaching 8.1937 kPa at 38.659 s. Pressure Gauge 2 reached its maximum value of 5.4834 kPa earlier at 36.264 s, while Pressure Gauges 3 and 4 reached 2.7179 kPa and 3.5777 kPa at 38.659 s.

At touchpoint ii), Pressure Gauge 1 again produced the highest recorded value, reaching 8.1413 kPa at 59.189 s. At the same time, Pressure Gauge 2 reached 6.4363 kPa and Pressure Gauge 3 reached 2.6483 kPa. Pressure Gauge 4 reached its maximum value for this event slightly earlier, with 3.5729 kPa at 57.821 s.

At touchpoint iii), the pressure response increased further. Pressure Gauge 1 reached 10.6407 kPa at 72.875 s, while Pressure Gauge 2 reached 8.7688 kPa at 72.533 s. Pressure Gauges 3 and 4 reached 3.4322 kPa and 5.4689 kPa at 72.533 s.

At touchpoint iv), the largest pressure values of the experiment were recorded. Pressure Gauge 1 reached 15.3932 kPa at 80.403 s, and Pressure Gauge 2 reached 13.8143 kPa at the same time. Pressure Gauges 3 and 4 reached their maximum values slightly earlier, with 11.0426 kPa and 12.4609 kPa at 80.061 s.

The results show that all four pressure gauges responded to each labelled touchpoint interaction, but the response magnitudes were different for each gauge. Pressure Gauge 1 recorded the highest value for all four touchpoints, while Pressure Gauge 3 generally showed the lowest response except during the final touchpoint event. This confirms that the pressure distribution within the gyroid-based pneumatic sensing structure was spatially non-uniform and that localized loading produced distinguishable pressure changes across the pressure gauge network.

6.5 Comparison of Empty, Sponge, and Gyroid Sensor Configurations

After evaluating the response of the gyroid-based sensor, additional experiments were performed to compare the effect of different internal structures on the pressure response. Three configurations were considered in this comparison: an empty sensor, a sponge-based sensor, and a gyroid-based sensor. The empty configuration was used as a control sample to evaluate the baseline pneumatic response without any internal structure. The sponge configuration was used as a conventional soft porous comparison, while the gyroid configuration represented the proposed structured sensing architecture.

Table 6.3: Sensor configurations used for the control comparison experiment.

Configuration	**Internal Structure**	**Purpose**
Empty sensor	No internal structure	Control sample for evaluating the baseline pneumatic response
Sponge sensor	Sponge-based porous structure	Comparison with a conventional soft porous material
Gyroid sensor	Gyroid TPMS structure	Evaluation of the proposed structured sensing architecture

Figure 6.5 shows the pressure response of the empty sensor configuration. This figure is used as the control case to evaluate the baseline pneumatic response without an internal structure.

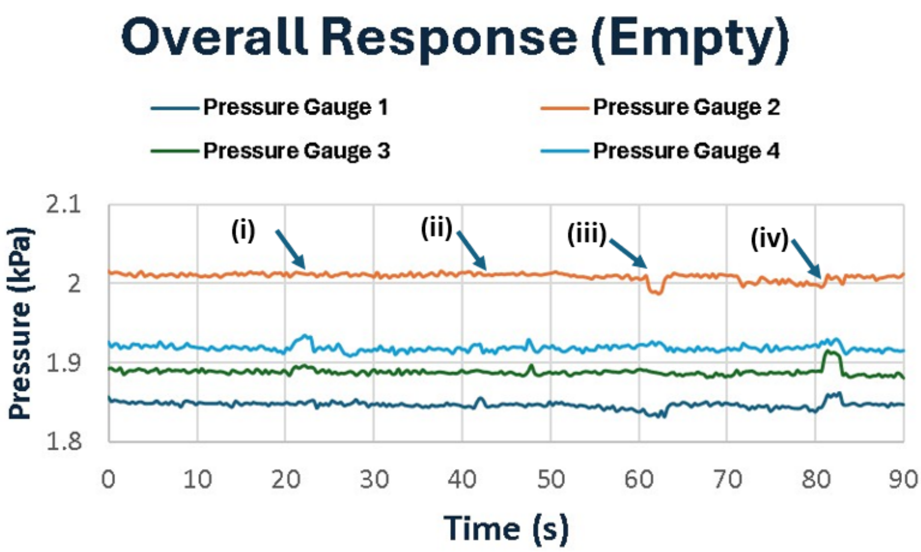

Figure 6.5: Pressure response of the empty sensor configuration under touchpoint loading.

Figure 6.6 shows the pressure response of the sponge-based sensor configuration.

This figure is used to compare the gyroid structure with a conventional soft porous material.

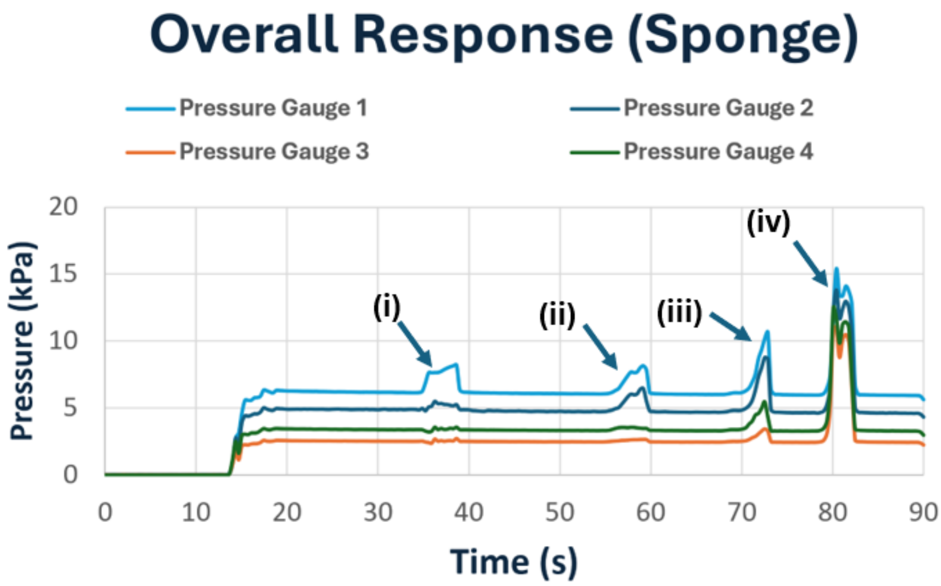

Figure 6.6: Pressure response of the sponge-based sensor configuration under touch-point loading.

Figure 6.7 shows the pressure response of the gyroid-based sensor configuration. This figure is used to evaluate the proposed structured sensing architecture under touchpoint loading.

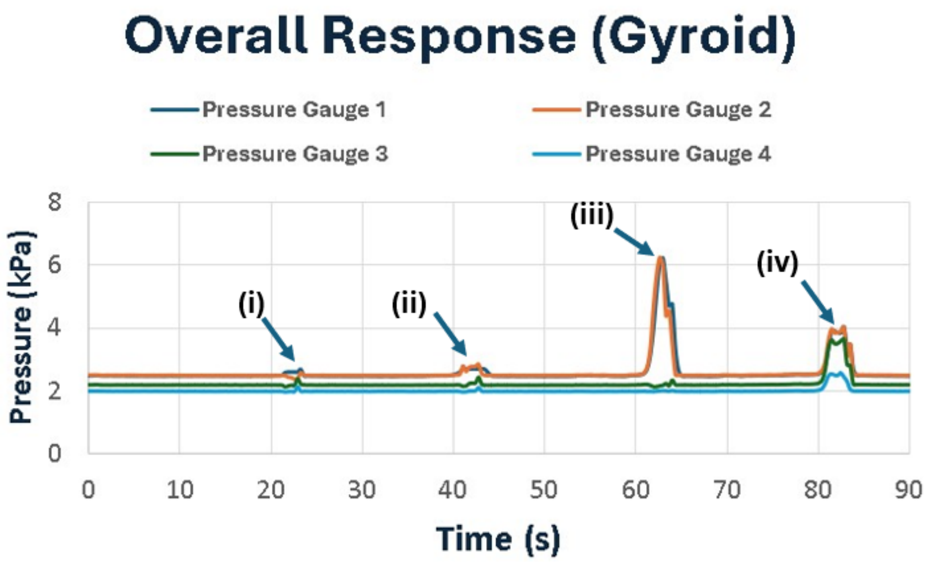

Figure 6.7: Pressure response of the gyroid-based sensor configuration under touch-point loading.

The comparison between the empty, sponge, and gyroid configurations shows that the internal architecture strongly influences the pressure response. The empty configuration produced the smallest response, with pressure values remaining close to the baseline throughout the experiment. This confirms that an empty pneumatic channel alone is not sufficient to generate a strong sensing response under localized loading.

The sponge-based configuration produced the largest pressure magnitudes. However, the response also contained a high baseline and larger signal variation, which may be caused by compression and recovery behaviour of the sponge material. Although the sponge sensor is sensitive to applied loading, its large baseline pressure and recovery characteristics may reduce its suitability for controlled and repeatable sensing applications.

The gyroid-based configuration produced clearer pressure peaks than the empty sensor while maintaining a more controlled response than the sponge sensor. The gyroid structure therefore provides a balance between sensitivity and signal stability.

The response peaks observed during touchpoint loading indicate that the deformation of the gyroid architecture can generate measurable pressure disturbances across multiple pressure gauges.

Table 6.4: Qualitative comparison of empty, sponge, and gyroid sensor configurations.

Configuration	**Signal**	**Response Stability**	**Observation**
Empty sensor	Very low	High	Limited sensitivity to localized loading
Sponge sensor	Very high	Moderate to low	Strong response, but higher baseline and larger fluctuations
Gyroid sensor	Moderate to high	High	Clear pressure peaks with controlled response

Based on this comparison in the table 6.4, the gyroid-based structure shows the most suitable behaviour for soft pneumatic sensing because it provides distinct pressure peaks without the excessive baseline shift observed in the sponge configuration. The empty sensor works as a useful control case, but it does not provide sufficient sensitivity. The sponge structure is highly sensitive, but its response is less controlled. In contrast, the gyroid structure provides a more balanced response, combining detectable pressure variation with structural repeatability and defined geometry.

6.5.1 Comparison of Gyroid Cell Size

A separate comparison was performed to evaluate the effect of gyroid cell size on the pressure response. Two gyroid configurations were considered: a gyroid structure with 0.7 mm cell size and a gyroid structure with 0.9 mm cell size. This comparison was used to investigate whether changing the internal gyroid geometry affects the magnitude and distribution of the pressure response.

Table 6.5: Gyroid cell-size configurations used in the comparative experiment.

Configuration	**Cell Size**	**Purpose**
Gyroid structure 1	0.7 mm	Evaluation of smaller gyroid cell size response
Gyroid structure 2	0.9 mm	Evaluation of larger gyroid cell size response

Table 6.5 summarizes the two gyroid cell-size configurations used in the comparative experiment. The table defines the 0.7 mm and 0.9 mm gyroid structures and their purpose in evaluating the effect of cell size on pressure response.

Figure 6.8 shows the pressure response of the gyroid sensor with a 0.7 mm cell size. This figure is used to evaluate the effect of a smaller gyroid cell size on the sensor response.

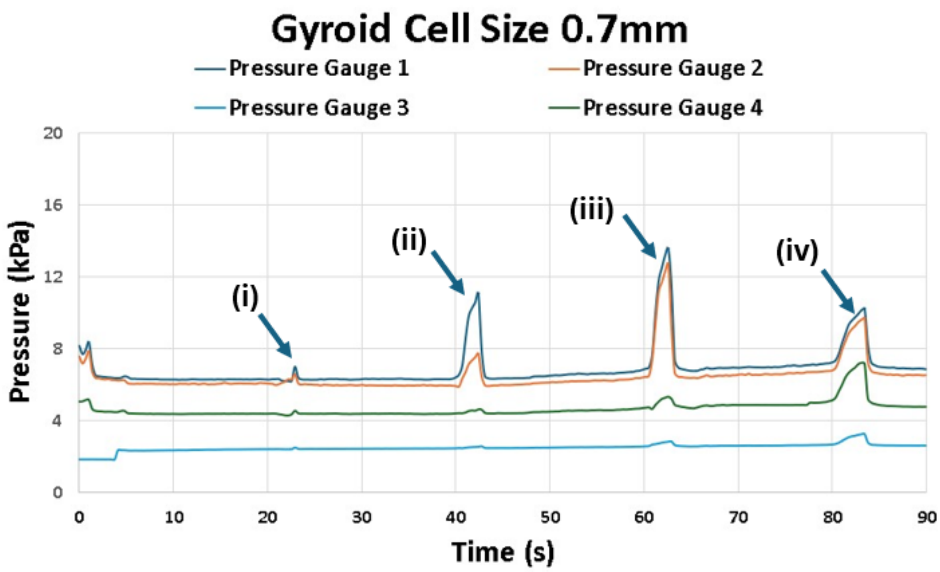

Figure 6.8: Pressure response of the gyroid sensor with 0.7 mm cell size.

The pressure response contains clear peaks during localized loading events, with Pressure Gauge 1 and Pressure Gauge 2 showing the strongest pressure changes. This suggests that the smaller cell size produces a sensitive response to local deformation.

The pressure response of the gyroid sensor with a 0.9 mm cell size, as shown in figure 6.9. This figure is used to evaluate the effect of a larger gyroid cell size on the sensor response.

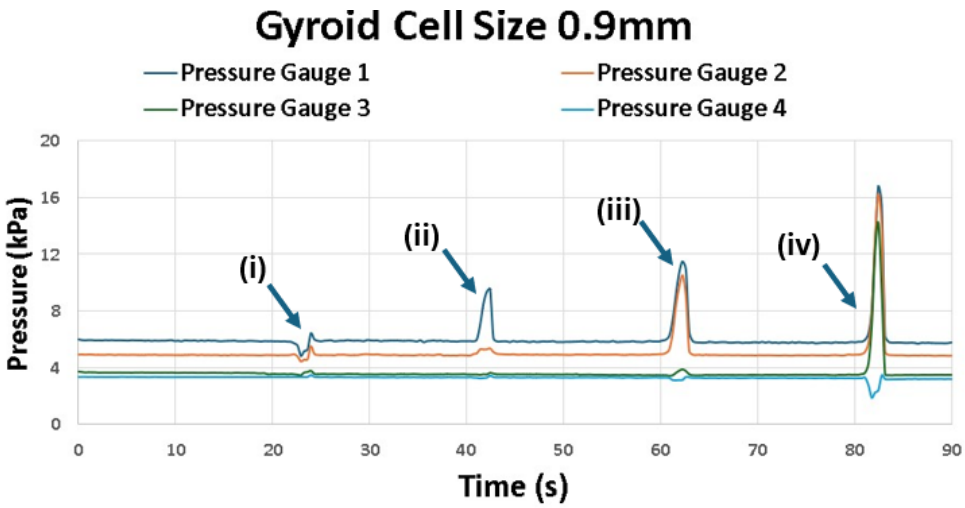

Figure 6.9: Pressure response of the gyroid sensor with 0.9 mm cell size.

The response also shows distinct pressure peaks during touchpoint interactions. Compared with the 0.7 mm gyroid, the 0.9 mm configuration shows a strong response at later touchpoints, indicating that cell size influences the pressure response and sensitivity of the structure.

The comparison between the 0.7 mm and 0.9 mm gyroid structures indicates that the internal geometry has a clear influence on the sensor response. Both gyroid structures produce measurable and distinguishable pressure peaks during loading. However, the relative magnitude of the response varies between pressure gauges and touchpoint locations, showing that cell size affects how deformation and airflow disturbances propagate through the structure.

The 0.7 mm gyroid structure shows strong sensitivity in Pressure Gauge 1 and Pressure Gauge 2, while the 0.9 mm gyroid structure shows stronger response peaks at later loading events. This suggests that smaller and larger cell sizes may influence the balance between local compliance, airflow restriction, and pressure transmission. Therefore, gyroid cell size can be treated as a design parameter for tuning the sensitivity and spatial response of pneumatic soft sensors.

6.6 Feasibility of Gyroid Structures for Pressure Sensing

Overall, the experimental results show that the system responds clearly to both pneumatic activation and localized touchpoint loading. The first rise in pressure corresponds to the activation of the pneumatic supply, which establishes the steady airflow condition through the gyroid sample. This continuous airflow is possible because the gyroid geometry provides interconnected internal pathways rather than isolated cavities. After this point, distinct touchpoint interactions generate additional pressure increases that are measured by all four pressure gauges.

The results also show that the four pressure gauges do not respond with identical magnitudes. Pressure Gauge 1 generally records the strongest response, while Pressure Gauge 3 records the lowest response. This confirms that the system is capable of capturing spatial pressure variation rather than only a single global pressure change. Therefore, the experimental results support the proof of concept that a gyroid-based pneumatic sensing region, combined with multiple pressure gauges, can be used to detect distributed touch interactions.

The comparison with empty and sponge-based configurations further supports the relevance of the gyroid structure. The empty configuration shows limited sensitivity, while the sponge configuration produces large but less controlled pressure variations. The gyroid structure provides a more balanced response by producing clear pressure peaks while maintaining a stable and structured sensing behaviour. This makes the gyroid architecture suitable for further development in soft robotic pressure sensing applications.

7 Conclusion

This thesis investigated the development of a soft pressure sensor for soft robotic applications. The work included the design and fabrication of gyroid structures, material characterization of Silicone 40A specimens, FE simulation of the gyroid specimen, and experimental pressure sensing demonstrations using multiple pressure gauges. The results showed that the gyroid structure can deform under applied loading while maintaining interconnected internal pathways for airflow, making it suitable as a soft internal sensing architecture.

The gyroid structures were successfully designed and fabricated as internal architectures for pneumatic sensing. The fabricated structures showed sufficient flexibility, which allowed them to deform under loading while maintaining connected airflow pathways. This confirmed that gyroid architectures can be used as functional internal structures.

The results of mechanical testing and simulation showed that the FE model could reasonably predict the general deformation behavior of the printed gyroid structure, especially in the initial and intermediate strain regions. Although deviations were observed at higher strain levels, that too due to the software limitations, the comparison confirmed that the simulation approach is useful for understanding the mechanical response of gyroid structures and supporting future design development.

The pressure sensing experiments demonstrated that localized touchpoint loading produced measurable pressure changes across the pressure gauge network. Compared with the empty configuration, the gyroid structure produced clearer pressure peaks, while compared with the sponge configuration, it showed a more controlled response. The comparison between different sizes of gyroid cells also showed that the internal geometry affects the pressure response and can be used as a design parameter to adjust the sensor behaviour.

Overall, the results support the feasibility of using gyroid architectures for pneumatic tactile pressure sensing. The study provides a basis for future development of a soft pneumatic gripper in which the soft pressure sensor can be integrated into the palm region or the finger region of the gripper. Future work can focus on testing the integrated gripper during practical grasping tasks, increasing the number of pressure gauges for better pressure distribution data, and using the response signals to train machine learning models. Such models could help identify the most informative pressure gauge locations and may reduce the total number of required pressure gauges while providing effective tactile sensing performance.

References

[1] S. Kim, C. Laschi, and B. Trimmer, "Soft robotics: A bioinspired evolution in robotics", en, *Trends in Biotechnology*, vol. 31, no. 5, pp. 287–294, May 2013, ISSN: 01677799. DOI: 10.1016/j.tibtech.2013.03.002. Accessed: Jan. 19, 2026. [Online]. Available: https://linkinghub.elsevier.com/retrieve/pii/S0167779913000632.

[2] Z. Chen et al., "Bioinspired and biohybrid soft robots: Principles and emerging technologies", *Matter*, vol. 8, no. 4, p. 102 045, Apr. 2025, ISSN: 25902385. DOI: 10.1016/j.matt.2025.102045. Accessed: Jun. 15, 2026.

[3] D. Trivedi, C. D. Rahn, W. M. Kier, and I. D. Walker, "Soft robotics: Biological inspiration, state of the art, and future research", English, *Applied Bionics and Biomechanics*, vol. 5, no. 3, pp. 99–117, 2008, ISSN: 1176-2322. DOI: 10.1080/11762320802557865.

[4] F. Ilievski, A. D. Mazzeo, R. F. Shepherd, X. Chen, and G. M. Whitesides, "Soft Robotics for Chemists", *Angewandte Chemie International Edition*, vol. 50, no. 8, pp. 1890–1895, 2011, _eprint: https://onlinelibrary.wiley.com/doi/pdf/10.1002/anie ISSN: 1521-3773. DOI: 10.1002/anie.201006464. Accessed: Jan. 21, 2026. [Online]. Available: https://onlinelibrary.wiley.com/doi/abs/10.1002/anie.201006464.

[5] C. Laschi, M. Cianchetti, B. Mazzolai, L. Margheri, M. Follador, and P. Dario, "Soft Robot Arm Inspired by the Octopus", *Advanced Robotics*, vol. 26, no. 7,

pp. 709–727, Jan. 2012, _eprint: https://doi.org/10.1163/156855312X626343, ISSN: 0169-1864. DOI: 10.1163/156855312X626343. Accessed: Jan. 22, 2026. [Online]. Available: https://doi.org/10.1163/156855312X626343.

[6] A. Marchese, R. Katzschmann, and D. Rus, "A Recipe for Soft Fluidic Elastomer Robots", *Soft Robotics*, vol. 2, pp. 7–25, Mar. 2015. DOI: 10.1089/soro.2014.0022.

[7] C. Thalman and P. Artemiadis, "A review of soft wearable robots that provide active assistance: Trends, common actuation methods, fabrication, and applications", *Wearable Technologies*, vol. 1, Sep. 2020. DOI: 10.1017/wtc.2020.4.

[8] D. Rus and M. T. Tolley, "Design, fabrication and control of soft robots", en, *Nature*, vol. 521, no. 7553, pp. 467–475, May 2015, ISSN: 1476-4687. DOI: 10.1038/nature14543. Accessed: Jan. 20, 2026. [Online]. Available: https://www.nature.com/articles/nature14543.

[9] *Design, fabrication and control of soft robots | Nature*. Accessed: Jan. 20, 2026. [Online]. Available: https://www.nature.com/articles/nature14543.

[10] B. Mosadegh et al., "Pneumatic Networks for Soft Robotics that Actuate Rapidly", en, *Advanced Functional Materials*, vol. 24, no. 15, pp. 2163–2170, 2014, _eprint: https://advanced.onlinelibrary.wiley.com/doi/pdf/10.1002/adfm.20130328 ISSN: 1616-3028. DOI: 10.1002/adfm.201303288. Accessed: Jan. 20, 2026. [Online]. Available: https://onlinelibrary.wiley.com/doi/abs/10.1002/adfm.201303288.

[11] E. W. Hawkes, L. H. Blumenschein, J. D. Greer, and A. M. Okamura, "A soft robot that navigates its environment through growth", *Science Robotics*, vol. 2, no. 8, eaan3028, Jul. 2017. DOI: 10.1126/scirobotics.aan3028. Accessed: Jan. 20, 2026. [Online]. Available: https://www.science.org/doi/10.1126/scirobotics.aan3028.

[12] *Multigait soft robot | PNAS*. Accessed: Jan. 20, 2026. [Online]. Available: https://www.pnas.org/doi/10.1073/pnas.1116564108.

[13] A. Koivikko, E. Sadeghian Raei, M. Mosallaei, M. Mantysalo, and V. Sariola, "Screen-Printed Curvature Sensors for Soft Robots", en, *IEEE Sensors Journal*, vol. 18, no. 1, pp. 223–230, Jan. 2018, ISSN: 1530-437X, 1558-1748, 2379-9153. DOI: 10.1109/JSEN.2017.2765745. Accessed: Jan. 20, 2026. [Online]. Available: https://ieeexplore.ieee.org/document/8080224/.

[14] *Electronics-free pneumatic circuits for controlling soft-legged robots | Science Robotics*. Accessed: Jan. 20, 2026. [Online]. Available: https://www.science.org/doi/10.1126/scirobotics.aay2627.

[15] *Digital logic for soft devices | PNAS*. Accessed: Jan. 20, 2026. [Online]. Available: https://www.pnas.org/doi/10.1073/pnas.1820672116.

[16] J.-H. Low, I. Delgado-Martinez, and C.-H. Yeow, "Customizable soft pneumatic chamber-gripper devices for delicate surgical manipulation", English, *Journal of Medical Devices, Transactions of the ASME*, vol. 8, no. 4, 2014, ISSN: 1932-6181. DOI: 10.1115/1.4027688.

[17] J.-y. Nagase, S. Wakimoto, T. Satoh, N. Saga, and K. Suzumori, "Design of a variable-stiffness robotic hand using pneumatic soft rubber actuators", en, *Smart Materials and Structures*, vol. 20, no. 10, p. 105 015, Aug. 2011, ISSN: 0964-1726. DOI: 10.1088/0964-1726/20/10/105015. Accessed: Jan. 19, 2026. [Online]. Available: https://doi.org/10.1088/0964-1726/20/10/105015.

[18] H. Matsuoka, T. K, a, S. Wakimoto, K. Suzumori, and P. Lambert, "Development of a Rubber Soft Actuator Driven with Gas/Liquid Phase Change", *International Journal of Automation Technology*, vol. 10, no. 4, pp. 517–524, Jul. 2016. DOI: 10.20965/ijat.2016.p0517. Accessed: Jan. 19, 2026. [Online]. Available: https://www.fujipress.jp/ijat/au/ijate001000040517/.

[19] G. Belforte et al., “Soft Pneumatic Actuators for Rehabilitation”, en, *Actuators*, vol. 3, no. 2, pp. 84–106, May 2014, ISSN: 2076-0825. DOI: 10.3390/act3020084. Accessed: Jan. 19, 2026. [Online]. Available: https://www.mdpi.com/2076-0825/3/2/84.

[20] N. Elango and A. A. M. Faudzi, “A review article: Investigations on soft materials for soft robot manipulations”, en, *The International Journal of Advanced Manufacturing Technology*, vol. 80, no. 5, pp. 1027–1037, Sep. 2015, ISSN: 1433-3015. DOI: 10.1007/s00170-015-7085-3. Accessed: Jan. 19, 2026. [Online]. Available: https://doi.org/10.1007/s00170-015-7085-3.

[21] A. Zolfagharian, A. Z. Kouzani, S. Y. Khoo, A. A. A. Moghadam, I. Gibson, and A. Kaynak, “Evolution of 3D printed soft actuators”, *Sensors and Actuators A: Physical*, vol. 250, pp. 258–272, Oct. 2016, ISSN: 0924-4247. DOI: 10.1016/j.sna.2016.09.028. Accessed: Jan. 20, 2026. [Online]. Available: https://www.sciencedirect.com/science/article/pii/S0924424716305064.

[22] F. Iida and C. Laschi, “Soft Robotics: Challenges and Perspectives”, *Procedia Computer Science*, Proceedings of the 2nd European Future Technologies Conference and Exhibition 2011 (FET 11), vol. 7, pp. 99–102, Jan. 2011, ISSN: 1877-0509. DOI: 10.1016/j.procs.2011.12.030. Accessed: Jan. 20, 2026. [Online]. Available: https://www.sciencedirect.com/science/article/pii/S1877050911006958.

[23] H. Shan*, X. Wang, Y. Jiang, and N. Xu, “Research on Lightweight Design and Performance Optimization of Lattice Structures Based on Additive Manufacturing”, *International Scientific Technical and Economic Research*, pp. 85–93, Nov. 2025, ISSN: 2959-1309, 2959-1309. DOI: 10.71451/ISTAER2556. Accessed: Feb. 2, 2026. [Online]. Available: https://www.istaer.online/index.php/Home/article/view/No.2556.

[24] A. Mohammed, D. Hamdan, and D. Ali, "Additive Manufacturing of Ceramic Components: A Review of 3D Printing Technologies for Industrial Applications", *Saudi Journal of Engineering and Technology*, vol. 11, pp. 1–22, Jan. 2026. DOI: 10.36348/sjet.2026.v11i01.001.

[25] Y. Song, S. Nesaei, D. Du, A. Gozen, and Y. Lin, "3D Printed Wearable Glucose Sensors", *ECS Meeting Abstracts*, vol. MA2018-01, pp. 2482–2482, Apr. 2018. DOI: 10.1149/MA2018-01/43/2482.

[26] S. Hasanov et al., "Review on Additive Manufacturing of Multi-Material Parts: Progress and Challenges", *Journal of Manufacturing and Materials Processing*, vol. 6, no. 1, p. 4, Dec. 27, 2021, ISSN: 2504-4494. DOI: 10.3390/jmmp6010004. Accessed: Mar. 9, 2026. [Online]. Available: https://www.mdpi.com/2504-4494/6/1/4.

[27] B. Berman, "3-D printing: The new industrial revolution", en, *Business Horizons*, vol. 55, no. 2, pp. 155–162, Mar. 2012, ISSN: 00076813. DOI: 10.1016/j.bushor.2011.11.003. Accessed: Feb. 2, 2026. [Online]. Available: https://linkinghub.elsevier.com/retrieve/pii/S0007681311001790.

[28] R. Bogue, "3D printing: The dawn of a new era in manufacturing?", English, *Assembly Automation*, vol. 33, no. 4, pp. 307–311, 2013, ISSN: 0144-5154. DOI: 10.1108/AA-06-2013-055.

[29] "3D Printing Disrupts Manufacturing: How Economies of One Create New Rules of Competition", en, *Research-Technology Management*, Accessed: Feb. 2, 2026. [Online]. Available: https://www.tandfonline.com/doi/abs/10.5437/08956308X5606193.

[30] E. R. Baker et al., "Mechanical properties of highly deformable elastomeric gyroids for multifunctional capacitors", *Advanced Engineering Materials*, vol. 25, p. 2 300 629, 2023. DOI: 10.1002/adem.202300629.

[31] H.-G. Kim, S. Hajra, H. J. Kim, H. Lee, and N. Kim, "Additively manufactured mechanical metamaterial-based pressure sensor with tunable sensing range and sensitivity", *Advanced Engineering Materials*, vol. 25, p. 2 201 499, 2023. DOI: 10.1002/adem.202201499.

[32] D. Huri, "Prediction Accuracy of Hyperelastic Material Models for Rubber Bumper under Compressive Load", *Polymers*, vol. 16, no. 17, p. 2534, Sep. 7, 2024, ISSN: 2073-4360. DOI: 10.3390/polym16172534. Accessed: May 19, 2026. [Online]. Available: https://www.mdpi.com/2073-4360/16/17/2534.

[33] L. He, S. Wang, and P. Maiolino, "Rubber-Like Soft Lattice Structure for Anti-Ballooning in Fluidic Elastic Soft Robots", *Advanced Engineering Materials*, vol. 25, no. 16, p. 2 300 534, Aug. 2023, ISSN: 1438-1656, 1527-2648. DOI: 10.1002/adem.202300534. Accessed: Mar. 9, 2026. [Online]. Available: https://advanced.onlinelibrary.wiley.com/doi/10.1002/adem.202300534.

[34] R. L. Truby et al., "Soft somatosensitive actuators via embedded 3d printing", *Advanced Materials*, vol. 30, no. 15, p. 1 706 383, 2018. DOI: 10.1002/adma.201706383.

[35] J.-B. Chossat, Y.-L. Park, R. J. Wood, and V. Duchaine, "A soft strain sensor based on ionic and metal liquids", *IEEE Sensors Journal*, vol. 13, no. 9, pp. 3405–3414, 2013. DOI: 10.1109/JSEN.2013.2251033.

[36] E. L. White, M. C. Yuen, J. C. Case, and R. K. Kramer, "Low-cost, facile, and scalable manufacturing of capacitive sensors for soft systems", *Advanced Materials Technologies*, vol. 2, no. 9, p. 1 700 072, 2017. DOI: 10.1002/admt.201700072.

[37] H. Xu et al., "An ultra-stretchable, highly sensitive and biocompatible capacitive strain sensor from an ionic nanocomposite for on-skin monitoring", *Nanoscale*, vol. 11, no. 4, pp. 1570–1578, 2019. DOI: 10.1039/C8NR08014C.

[38] H. Zhao, K. O'Brien, S. Li, and R. F. Shepherd, "Optoelectronically innervated soft prosthetic hand via stretchable optical waveguides", *Science Robotics*, vol. 1, no. 1, eaai7529, 2016. DOI: 10.1126/scirobotics.aai7529.

[39] A. Leber et al., "Stretchable thermoplastic elastomer optical fibers for sensing of extreme deformations", *Advanced Functional Materials*, vol. 29, no. 15, p. 1 802 629, 2019. DOI: 10.1002/adfm.201802629.

[40] R. Goldoni et al., "Stretchable nanocomposite sensors, nanomembrane interconnectors, and wireless electronics toward feedback-loop control of a soft earthworm robot", *ACS Applied Materials & Interfaces*, vol. 12, no. 39, pp. 43 388–43 397, 2020. DOI: 10.1021/acsami.0c11812.

[41] Y. Mengüc et al., "Wearable soft sensing suit for human gait measurement", *The International Journal of Robotics Research*, vol. 33, no. 14, pp. 1748–1764, 2014. DOI: 10.1177/0278364914546072.

[42] H. Yang, Y. Chen, Y. Sun, and L. Hao, "A novel pneumatic soft sensor for measuring contact force and curvature of a soft gripper", *Sensors and Actuators A: Physical*, vol. 266, pp. 318–327, Oct. 2017, ISSN: 09244247. DOI: 10.1016/j.sna.2017.09.040. Accessed: Mar. 9, 2026. [Online]. Available: https://linkinghub.elsevier.com/retrieve/pii/S0924424717311597.

[43] P. Polygerinos et al., "Soft robotics: Review of fluid-driven intrinsically soft devices; manufacturing, sensing, control, and applications in human-robot interaction", *Advanced Engineering Materials*, vol. 19, no. 12, p. 1 700 016, 2017. DOI: 10.1002/adem.201700016.

[44] B. Mosadegh et al., "Pneumatic networks for soft robotics that actuate rapidly", *Advanced Functional Materials*, vol. 24, no. 15, pp. 2163–2170, 2014. DOI: 10.1002/adfm.201303288.

[45] O. Al-Ketan and R. K. Abu Al-Rub, "Multifunctional Mechanical Metamaterials Based on Triply Periodic Minimal Surface Lattices", *Advanced Engineering Materials*, vol. 21, no. 10, p. 1 900 524, Oct. 2019, ISSN: 1438-1656, 1527-2648. DOI: 10.1002/adem.201900524. Accessed: Mar. 9, 2026. [Online]. Available: https://advanced.onlinelibrary.wiley.com/doi/10.1002/adem.201900524.

[46] J. Feng, J. Fu, X. Yao, and Y. He, "Triply periodic minimal surface (TPMS) porous structures: From multi-scale design, precise additive manufacturing to multidisciplinary applications", *International Journal of Extreme Manufacturing*, vol. 4, no. 2, p. 022 001, Jun. 1, 2022, ISSN: 2631-8644, 2631-7990. DOI: 10.1088/2631-7990/ac5be6. Accessed: Mar. 9, 2026. [Online]. Available: https://iopscience.iop.org/article/10.1088/2631-7990/ac5be6.

[47] M. S. Hossain, M. M. Hossain, and S. Nilufar, "An Overview of Additive Manufacturing of Triply Periodic Minimal Surface (TPMS) Structures", *Polymers*, vol. 17, no. 24, p. 3307, Dec. 14, 2025, ISSN: 2073-4360. DOI: 10.3390/polym17243307. Accessed: Mar. 9, 2026. [Online]. Available: https://www.mdpi.com/2073-4360/17/24/3307.

[48] D. Morales, E. Palleau, M. D. Dickey, and O. D. Velev, "Electro-actuated hydrogel walkers with dual responsive legs", en, *Soft Matter*, vol. 10, no. 9, pp. 1337–1348, Feb. 2014, ISSN: 1744-6848. DOI: 10.1039/C3SM51921J. Accessed: Jan. 19, 2026. [Online]. Available: https://pubs.rsc.org/en/content/articlelanding/2014/sm/c3sm51921j.

[49] M. Shahzad, A. Kamran, M. Z. Siddiqui, and M. Farhan, "Mechanical Characterization and FE Modelling of a Hyperelastic Material", *Materials Research*, vol. 18, no. 5, pp. 918–924, Oct. 2015, ISSN: 1516-1439. DOI: 10.1590/1516-1439.320414. Accessed: May 19, 2026.

[50] M. Mooney, “A Theory of Large Elastic Deformation”, *Journal of Applied Physics*, vol. 11, no. 9, pp. 582–592, Sep. 1940, ISSN: 0021-8979, 1089-7550. DOI: 10.1063/1.1712836. Accessed: May 19, 2026.

[51] R. S. Rivlin, “Large elastic deformations of isotropic materials IV. further developments of the general theory”, *Philosophical Transactions of the Royal Society of London. Series A, Mathematical and Physical Sciences*, vol. 241, no. 835, pp. 379–397, Oct. 1948, ISSN: 0080-4614, 2054-0272. DOI: 10.1098/rsta.1948.0024. Accessed: May 19, 2026.

[52] R. W. Ogden, “Large deformation isotropic elasticity – on the correlation of theory and experiment for incompressible rubberlike solids”, *Proceedings of the Royal Society of London. A. Mathematical and Physical Sciences*, vol. 326, no. 1567, pp. 565–584, Feb. 1972, ISSN: 0080-4630, 2053-9169. DOI: 10.1098/rspa.1972.0026. Accessed: May 19, 2026.

[53] O. H. Yeoh, “Some Forms of the Strain Energy Function for Rubber”, *Rubber Chemistry and Technology*, vol. 66, no. 5, pp. 754–771, Nov. 1993, ISSN: 1943-4804, 0035-9475. DOI: 10.5254/1.3538343. Accessed: May 19, 2026.

[54] C. Güdür, T. Türkoğlu, and İ. Eren, “Effect of Lattice Design and Process Parameters on the Properties of PLA, ABS AND PETG Polymers Produced by Fused Deposition Modelling”, *Journal of Materials and Mechatronics: A*, vol. 4, no. 2, pp. 561–570, Dec. 26, 2023, ISSN: 2717-8811. DOI: 10.55546/jmm.1357217. Accessed: Mar. 9, 2026. [Online]. Available: http://dergipark.org.tr/en/doi/10.55546/jmm.1357217.

[55] M. Araya, M. Jaskari, T. Rautio, T. Guillén, and A. Järvenpää, “Assessing the compressive and tensile properties of TPMS-Gyroid and stochastic Ti64 lattice structures: A study on laser powder bed fusion manufacturing for biomedical implants”, *Journal of Science: Advanced Materials and Devices*, vol. 9, no. 1,

p. 100 663, Mar. 2024, ISSN: 24682179. DOI: 10.1016/j.jsamd.2023.100663. Accessed: May 19, 2026.

[56] Honeywell International Inc., *Abp2 series board mount pressure sensors datasheet*, Accessed: 2026-03, 2023. [Online]. Available: https://prod-edam.honeywell.com/content/dam/honeywell-edam/sps/siot/en-us/products/sensors/pressure-sensors/board-mount-pressure-sensors/abp2-series/documents/sps-siot-abp2-series-datasheet.pdf.